International Journal of Solids and Structures 132–133 (2018) 171–187

Contents lists available at ScienceDirect

International Journal of Solids and Structures

journal homepage: www.elsevier.com/locate/ijsolstr

Mechanical properties and failure mechanisms of sandwich panels with ultra-lightweight three-dimensional hierarchical lattice cores

Qianqian Wu[a], Ying Gao[a], Xingyu Wei[a], Davood Mousanezhad[b], Li Ma[a], Ashkan Vaziri[b], Jian Xiong[a,*]

[a] Center for Composite Materials and Structures, Harbin Institute of Technology, Harbin 150001, PR China
[b] Department of Mechanical and Industrial Engineering, Northeastern University, Boston, MA 02115, USA

ARTICLE INFO

Article history:
Received 2 April 2017
Revised 30 August 2017
Available online 21 September 2017

Keywords:
Lattice core
Hierarchical structure
Sandwich panel
Mechanical properties
Failure mechanism map

ABSTRACT

Mechanical properties and failure mechanisms of sandwich panels with "corrugated-pyramidal" hierarchical lattice cores were investigated through analytical modeling and detailed numerical simulations. This included studying the behavior of hierarchical lattice core material under compression and shearing, as well as investigating the mechanical performance of sandwich panels subjected to in-plane compression and three-point bending. Failure maps were constructed for the hierarchical lattice cores, as well as sandwich panels with hierarchical lattice cores by deriving analytical closed-form expressions for strength for all possible failure modes under each loading. 3D printed samples were manufactured and tested under out-of-plane compression in order to provide limited experimental validation of the study. Our study provides insights into the role of structural hierarchy in tuning the mechanical behavior of sandwich structures, and new opportunities for designing ultra-lightweight lattice cores with optimal performance.

1. Introduction

Unique mechanical properties, as well as multifunctional advantages offered by lattice materials with open-cell configurations make them an attractive choice for designing and constructing lightweight multifunctional structures (Roper, 2011; Barnett et al., 2001; Evans, 2001; Ashby, 2001; Wei et al., 2016; Zok et al., 2016). In this context, numerical simulations and theoretical studies have been previously employed to investigate the effects of geometry, mass density, and structural defects on mechanical properties (Ajdari et al., 2008) and deformation (Liao et al., 2014; Wang et al., 2013) of two-dimensional periodic lattice materials. The effects of temperature on the mechanical properties of composite sandwich structures also have been studied through experiments (Liu et al., 2014, 2015). Currently, various types of three-dimensional periodic truss sandwich structures with high specific strength and high specific stiffness have emerged and their superior mechanical properties have been broadly recognized (Vaziri and Xue, 2007; Ajdari et al., 2011; Lim and Kang, 2006; Liu et al., 2007; Dong et al., 2015; Schaedler et al., 2011). Introducing hierarchy in the structural organization of lattice materials can potentially improve their mechanical and multifunctional properties (Han et al., 2015; Xiong et al., 2015; Mousanezhad et al., 2015, 2016). Lakes (1993) is amongst the pioneers in investigating the role of structural hierarchy in the mechanical properties of natural and man-made materials. Taking wood (Deshpande et al., 2006) and bone (Weaver et al., 2007) as examples of biological materials with hierarchical architecture, their internal microstructure is composed of tiny truss-like elements contributing to their enhanced energy absorption and anti-vibration characteristics. Even at nanoscales, it has been shown that carbon nanotube ropes with hierarchical helical structures exhibit superior properties such as larger failure strain, easily tunable elastic properties, and higher energy storage ability compared to bundles of straight nanotubes (Zhao et al., 2014). Therefore, integrating the concept of structural hierarchy with man-made lattice structures has a potential of improve their mechanical performance.

In this context, structural hierarchy has been recently integrated into honeycomb structures to broaden the achievable range of elastic and plastic responses (Ajdari et al., 2012; Mousanezhad et al., 2016; Haghpanah et al., 2013, 2014; Oftadeh et al., 2014a,b). The results show that honeycombs with 1st and 2nd orders of hierarchy are capable of attaining specific Young's modulus as much as 2 and 3.5 times that of a regular honeycomb with the same mass (Ajdari et al., 2012), and can further be increased at higher levels of hierarchy (Oftadeh et al., 2014a,b). Recently, structural hierarchy has been shown to induce the unusual "auxetic" property (i.e.,

* Corresponding author.
E-mail address: jx@hit.edu.cn (J. Xiong).

https://doi.org/10.1016/j.ijsolstr.2017.09.024
0020-7683/

negative Poisson's ratio) in honeycombs (Mousanezhad et al., 2015), and enhance the phononic properties of these materials (Mousanezhad et al., 2016).

In another set of studies, analytical, numerical, and experimental investigations are carried out to study the mechanical performance of hierarchical corrugated composite sandwich cores under out-of-plane compressive and in-plane shearing loads (Kazemahvazi et al., 2009; Kazemahvazi and Dan, 2009). Again, structural hierarchy has been shown to increase the effective compressive strength up to seven times greater than those of non-hierarchical structures with the same mass at small relative densities. Although introducing hierarchy increases manufacturing complexity (compared with 1st order lattice structures), it is also shown to have significant potential in improving the structural performance of cellular materials (Ajdari et al., 2012; Kazemahvazi et al., 2009; Oftadeh et al., 2014a,b).

Under dynamic loading, hierarchical periodic truss sandwich structures exhibit enhanced anti-crushing behavior and higher specific energy absorption (Zhang et al., 2013; Fan et al., 2014; Qiao and Chen, 2016; Sun et al., 2016a,b). Yang et al. (2016) introduce a novel hybrid foam-core/solid-shell structure that inherits the advantages of their constituent components (i.e., conventional foam and solid-shell structure), in both strength and deformation, and can obtain high energy absorption capability. Inspired by a luffa sponge hierarchical bio-cellular topology, An and Fan (2016) propose a hierarchical aluminum foam cylinder, reinforced by stiff thin-walled carbon fiber reinforced plastic (CFRP) tubes, and show that the interaction between the CFRP tubes and aluminum foam results in an increase in the specific energy absorption of the hierarchical cylinder.

According to the literature (summarized above), studies on the mechanical properties of hierarchical lattice core constructions have been limited to out-of-plane compression and shear loading, and analytical modeling of these structures under lateral compressive and three-point bending loads has not yet been explored. Here, we investigate the mechanical performance of the "corrugated-pyramidal" lattice truss structures under out-of-plane and transverse compression, shear, and three-point bending. To this end, we first introduce the geometry of these hierarchical structures which are based on pyramidal lattice structures introduced earlier by Wu et al. (2016). Based on the recently established terminology and taxonomy for periodic truss structures (Zok et al., 2016), our geometry is classified as "compound cubic truss". Next, we derive closed-form expressions for the structural strength associated with different possible failure modes, and construct failure maps for sandwich panels with hierarchical lattice core construction. The effects of structural hierarchy are highlighted by comparing the results with those of non-hierarchical counterparts (of same mass).

2. Geometry of hierarchical lattice core

The original non-hierarchical structure is composed of the 1st order "corrugated-pyramidal" truss core sandwiched between the 1st order face sheets, while the 2nd order structure is achieved by replacing each 1st order truss element with the 2nd order face sheets and a 2nd order corrugated pyramidal truss core, Fig. 1. Here, for the sake of brevity, the 1st and 2nd order lattice cores are referred to as core I and II, respectively. Fig. 1 shows a schematic diagram of geometrical characteristics of the unit cells of the original and 2nd order structures, where b and b_f are the width of the 1st and 2nd order face sheets, and t_f and t_c are face sheet and strut thickness of the 2nd order structure in core II, respectively. In addition, l and l_c are the strut length of core I and core II, respectively, and ω and ω_c are the angles which core I and II struts make with their corresponding face sheets, respectively. Finally, α, and β are the angles which core I makes with axis 1 and axis 2. The relative density, ρ, defined as the ratio of the density of the "corrugated-pyramidal" core ρ_c to that of the parent carbon fiber composite, ρ_{cf}, is calculated by

$$\bar{\rho} = \frac{2A_a\left(2t_f\cos\omega + t_c\right)}{l^2 l_c \cos^3\omega \sin^2\omega}, \tag{1}$$

where $A_a = b_f(l_c \sin\omega_c + t_f)$ denotes the cross-sectional area of the 1st order lattice core.

3. Out-of-plane compression of lattice core

3.1. Stiffness

With reference to the method presented by Chen et al. (2012), the equivalent out-of-plane compressive stiffness of the "corrugated-pyramidal" 2nd order lattice truss, normalized by the Young's modulus of the parent material, is (see Appendix for details)

$$\frac{\bar{E}}{E} = \frac{2\xi_\omega A_\mathrm{I}\sin^2\omega}{l^2\cos^2\omega}, \tag{2}$$

where ξ_ω is a non-dimensional parameter, and its corresponding expression is

$$\xi_\omega = \sin\omega + \frac{12(EI)_\mathrm{I}\cos^2\omega}{(EA)_\mathrm{I} l^2 \sin\omega}. \tag{3}$$

In Eq. (3), $(EA)_\mathrm{I}$ and $(EI)_\mathrm{I}$ are equivalent compressive stiffness and flexural rigidity of core I, respectively, which can be obtained using the following equations.

$$(EA)_\mathrm{I} = 2Eb_f t_f + Eb_f \frac{t_c^3}{l_c^2}\sin^2\omega_c \cos\omega_c + Eb_f t_c \cos^3\omega_c, \tag{4}$$

$$(EI)_\mathrm{I} = \frac{1}{6}Eb_f t_f^3 + \frac{1}{2}\left(l_c\sin\omega_c + t_f\right)^2 Eb_f t_f + \frac{1}{4}\sin^2\omega_c\cos^3\omega_c l_c^2 Eb_f t_c + \frac{1}{12}\mathrm{f}(\omega_c)Eb_f t_c^3, \tag{5}$$

where $\mathrm{f}(\omega_c) = \cos\omega_c + 3\sin^2\omega_c\cos\omega_c - 3\sin^2\omega_c\cos^3\omega_c$.

To validate these analytical expressions, finite element (FE) based numerical simulations were conducted using commercial software ABAQUS 6.13-2 (SIMULIA, Providence, RI). Six different types of structures with various relative densities and geometrical characteristics were considered for numerical simulations, Table 1. The parent material was assumed to be a carbon fiber-reinforced composite with effective compressive stiffness and strength of 100 GPa and 850 MPa, and Poisson's ratio of 0.3.

We performed FE analysis for the lattice core unit cell, shown in Fig. 1. In the simulations, rigid face sheets were tied to the lattice core structure at the interface nodes. While the bottom face sheet was fixed, a compressive displacement was then applied to the top face sheet to simulate core crushing. The models were meshed using three-dimensional 8-node linear brick elements with reduced integration (i.e., C3D8R element in ABAQUS), and a mesh sensitivity analysis was performed to guarantee that the results were not mesh-dependent. Static-general solver of ABAQUS was used to simulate the response of structures under compressive loads.

Fig. 2 plots the normalized equivalent out-of-plane compressive stiffness of the 1st and 2nd order lattice trusses as a function of the relative density. The dashed and solid lines show the analytical expression presented by Eq. (2), respectively, while the markers denote the FE results for the 1st and 2nd order structures. An excellent agreement is observed between the analytical and FE results. The results presented in Fig. 2 shows that the equivalent out-of-plane compressive stiffness of the "corrugated-pyramidal"

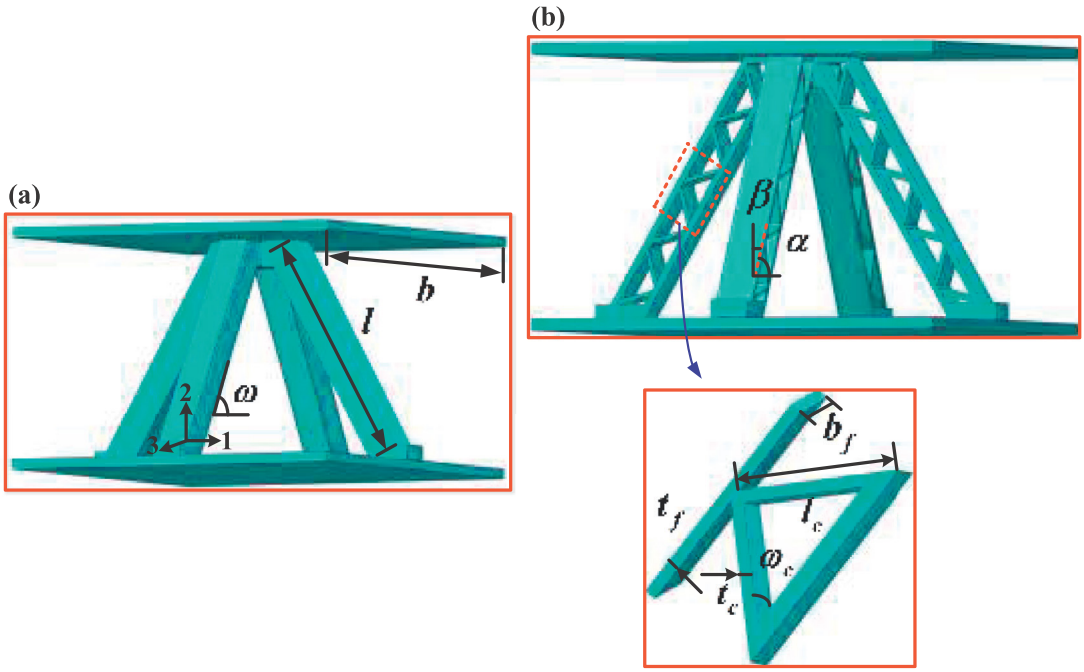

Fig. 1. Unit cell of the 1st order pyramidal (a) and "corrugated-pyramidal" 2nd order lattice truss (b) with corresponding geometric parameters.

Table 1
Dimensions of the six typical specimens for compressive stiffness simulations.

Structural topologies	Relative density (%) ($\bar{\rho}$)	Truss-I (mm) ($l \times b_f \times t_f$)	Truss-II (mm) ($l_c \times b_f \times t_c$)
1st order	0.21	41.48 × 1.07 × 0.67	/
2nd order		41.48 × 1.07 × 0.33	1.33 × 1.07 × 0.067
1st order	0.37	270.54 × 13.04 × 4.53	/
2nd order		270.54 × 13.04 × 2.17	8.7 × 13.04 × 0.43
1st order	0.67	177.78 × 8.57 × 2.98	/
2nd order		177.78 × 8.57 × 2.86	5.71 × 8.57 × 0.28
1st order	1.04	75 × 6.02 × 2.37	/
2nd order		75 × 6.02 × 1.2	2.41 × 6.02 × 0.12
1st order	1.2	622.25 × 60 × 19.73	/
2nd order		622.5 × 60 × 10	20 × 60 × 1
1st order	1.55	480.83 × 48 × 19.76	/
2nd order		480.83 × 48 × 10	15 × 48 × 1

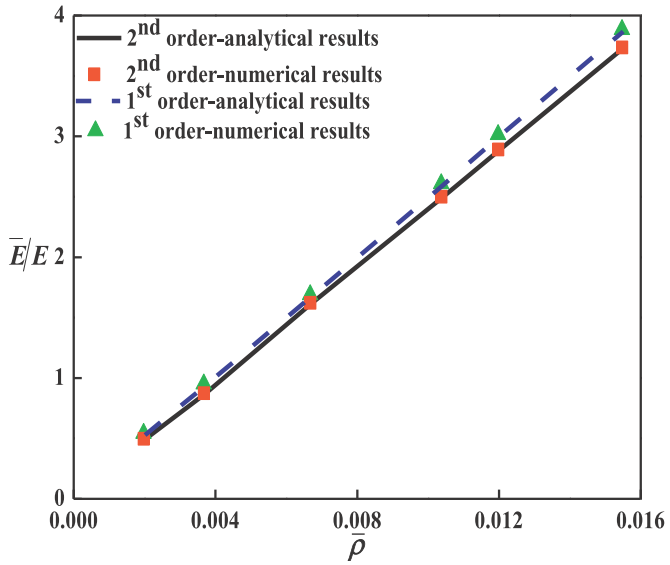

Fig. 2. Comparisons of compressive stiffness between the 2nd order lattice truss and the 1st order pyramidal truss with different relative densities.

2nd order lattice truss is slightly lower compared to its 1st order counterpart. In contrast to the 1st order pyramidal truss in which the deformation is uniformly distributed between all truss members, for the "corrugated-pyramidal" 2nd order lattice truss, the majority of the load is carried by the 2nd order face sheets, and the 2nd order truss members make relatively small contribution to the overall stiffness of the structure.

3.2. Strength

Five competing failure modes for the "corrugated-pyramidal" 2nd order lattice truss structures subjected to compression were considered, as shown in Fig. 3. Appendix A provides further details with regards to these failure modes. Note that we assume that the 2nd order face sheets are made of a material that exhibits plastic yielding after the initial elastic regime.

3.2.1. Face sheet wrinkling (FW) of the 2nd order lattice truss

This failure mode, shown in Fig. 3(b), is characterized by localized short wavelength elastic buckling (or wrinkling) of the face sheets of the 2nd order lattice truss between adjacent nodes. Thus, the critical load of buckling of the face sheet, F_f, is (see Appendix

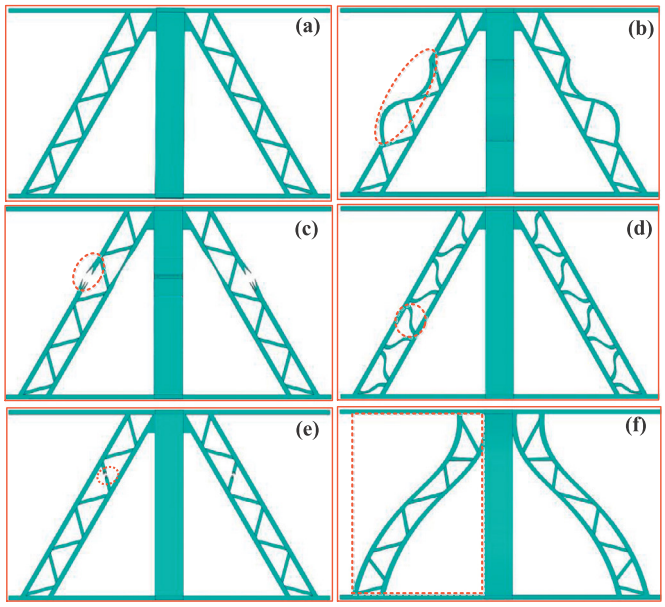

Fig. 3. Failure modes of the "corrugated-pyramidal" 2nd order lattice truss: (a) "Corrugated-pyramidal" structural hierarchy; (b) Face sheet wrinkling (FW) of the 2nd order lattice truss; (c) Face sheet crushing (FC) of the 2nd order lattice truss; (d) Core member buckling (CE) of the 2nd order lattice truss; (e) Core member crushing (CC) of the 2nd order lattice truss; (f) Macro Euler buckling of the 1st order pyramidal truss.

for details)

$$F_f = \frac{\pi^2 (EI)_{\mathrm{I}}^f}{2\mu^2 {l_c}^2 \cos^2\omega_c}, \tag{6}$$

where parameter, μ, depends on the conditions of end constraints of the buckled struts. For instance, $\mu = 0.5$ describes a condition at which one end is clamped (i.e., fixed) and the other end is pinned (see Appendix Fig. A-1 for details). Moreover, $(EI)_{\mathrm{I}}^f$ denotes the flexural rigidity of the 2nd order face sheets, $(EI)_{\mathrm{I}}^f = Eb_f {t_f}^3/12$. The relation between the critical load of buckling of the 2nd order face sheet, F_f, and the axial load along core I, F_A, is

$$F_A = (1+\zeta_c) F_f, \tag{7}$$

where

$$\zeta_c = \frac{(EA)_{\mathrm{II}} \cos^3\omega_c}{2(EA)_{\mathrm{I}}^f} + \frac{6(EI)_{\mathrm{II}} \cos\omega_c \sin^2\omega_c}{(EA)_{\mathrm{I}}^f {l_c}^2}. \tag{8}$$

The compressive stiffness of the 2nd order face sheets, and compressive stiffness and flexural rigidity of core II are

$$(EA)_{\mathrm{I}}^f = Eb_f t_f, \tag{9}$$

$$(EA)_{\mathrm{II}} = Eb_f t_c, \tag{10}$$

$$(EI)_{\mathrm{II}} = \frac{Eb_f {t_c}^3}{12}. \tag{11}$$

Now, using Eqs. (9)–(11), Eq. (8) reduces to

$$\zeta_c = \frac{t_c^3 \sin^2\omega_c \cos\omega_c + t_c l_c^2 \cos^3\omega_c}{2 t_f l_c^2}. \tag{12}$$

Also, substituting Eq. (6) into Eq. (7) gives the axial load along core I as

$$F_A = \frac{(1+\zeta_c)\pi^2 E b_f {t_f}^3}{6 {l_c}^2 \cos^2\omega_c}, \tag{13}$$

by using which the equivalent out-of-plane compressive strength of the unit cell is calculated by

$$\overline{\sigma} = \frac{\xi_\omega (1+\zeta_c)\pi^2 E b_f {t_f}^3}{3 l^2 {l_c}^2 \cos^2\omega \cos^2\omega_c}. \tag{14}$$

3.2.2. Face sheet crushing (FC) of the 2nd order lattice truss

This failure mode is achieved by face sheet crushing of the 2nd order lattice truss (rather than elastic buckling), Fig. 3c. We define the collapse strength of the parent material as, σ_f, thus the critical load associated with face sheet crushing, F_f, is

$$F_f = 2 b_f t_f \sigma_f. \tag{15}$$

Now, by substituting Eq. (15) into Eq. (7), the axial load, F_A, is

$$F_A = 2(1+\zeta_c) b_f t_f \sigma_f, \tag{16}$$

which can further be used to obtain the equivalent out-of-plane compressive strength of the unit cell with the following expression:

$$\overline{\sigma} = \frac{4\xi_\omega (1+\zeta_c) b_f t_f \sigma_f}{l^2 \cos^2\omega}. \tag{17}$$

3.2.3. Core member buckling (CE) of the 2nd order lattice truss

Under out-of-plane compressive loads, the 2nd order lattice truss can undergo Euler buckling (Hearn, 1997) as shown schematically in Fig. 3(d). The critical load of buckling is then calculated by (see Appendix for details)

$$F_c = \frac{\pi^2 (EI)_{\mathrm{II}}}{\mu^2 {l_c}^2}, \tag{18}$$

where again the parameter μ is assumed to be equal to 0.5 considering one end of the strut to be clamped and the other end as a pin support. Then, the relationship between the axial load, F_c, along core II and in-plane compressive force, F_A, is

$$F_A = \lambda_c F_c, \tag{19}$$

where

$$\lambda_c = \cos\omega_c + \frac{2(EA)_{\mathrm{I}}^f}{(EA)_{\mathrm{II}} \cos^2\omega_c} + \frac{12(EI)_{\mathrm{II}} \sin^2\omega_c}{(EA)_{\mathrm{II}} {l_c}^2 \cos\omega_c}. \tag{20}$$

Now, substituting Eqs. (9)–(11) into Eq. (20) gives

$$\lambda_c = \cos\omega_c + \frac{t_c^2 \sin^2\omega_c}{l_c^2 \cos\omega_c} + \frac{2t_{\mathrm{f}}}{t_c \cos^2\omega_c}. \tag{21}$$

Then, according to the relation between the axial force of the corrugated core and the out-of-plane compressive load, which are shown in Eqs. (A-31) and (A-34) in the Appendix, closed-form expression of equivalent out-of-plane compressive strength of the unit cell can be obtained as

$$\overline{\sigma} = \frac{2\xi_\omega \lambda_c \pi^2 E b_f {t_c}^3}{3 l^2 {l_c}^2 \cos^2\omega}. \tag{22}$$

3.2.4. Core member crushing (CC) of the 2nd order lattice truss

This failure mode is characterized by crushing of the 2nd order truss members, Fig. 3e, where the critical load of failure is

$$F_c = b_f t_c \sigma_f. \tag{23}$$

Then, similar to the previous calculations, $F_A = \lambda_c F_c$, and equivalent out-of-plane compressive strength of the unit cell is

$$\overline{\sigma} = \frac{2\xi_\omega \lambda_c b_f t_c \sigma_f}{l^2 \cos^2\omega}. \tag{24}$$

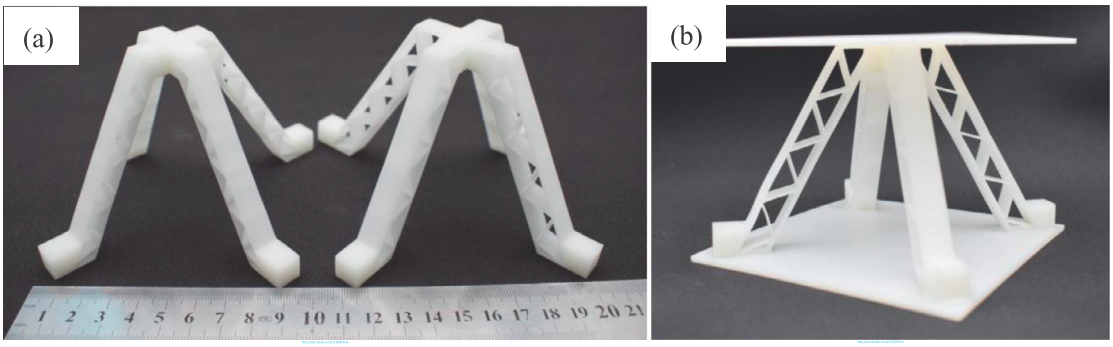

Fig. 4. "Corrugated-pyramidal" 2nd order lattice truss structure without the face sheets (a) and with the face sheets (b), fabricated using 3D printing.

3.2.5. Euler buckling of the 1st order pyramidal truss

Fig. 3(f) shows a schematic diagram of Euler buckling (Hearn, 1997) of the 1st order pyramidal truss members, where the critical load, F_{cr}, is

$$F_{cr} = \frac{\pi^2 (EI)_1}{\mu^2 l^2}, \tag{25}$$

with $\mu = 0.5$. Then, the equivalent out-of-plane compressive strength of the unit cell is calculated by

$$\overline{\sigma} = 8\xi_\omega \frac{\pi^2 (EI)_1}{l^4 \cos^2\omega}. \tag{26}$$

3.3. Experiments

To validate the results presented in the previous sections, we performed a limited number of compression tests on 3D printed samples of the "corrugated-pyramidal" 2nd order lattice truss structures – Fig. 4. We performed separate tests on dog-bone samples of the parent material to characterize the material properties. The stiffness and strength of the parent material were obtained as 2.56 GPa and 26.62 MPa, respectively.

During the experiments, the applied compressive load was measured by an INSTRON 5569 machine, while a laser extensometer (Epsilon) was used to measure the nominal compressive displacement. The compression tests were carried out in the quasi-static regime with a nominal displacement rate of 0.5 mm/min at room temperature. A minimum of three tests were conducted to ensure the repeatability of the results. The geometrical parameters of these samples as well as the corresponding failure modes are given in Table 3. The experimental results clearly demonstrate the failure modes presented above.

4. Out-of-plane shearing of 2nd order lattice truss structure

4.1. Stiffness

The equivalent shear stiffness of the "corrugated-pyramidal" 2nd order lattice truss structure can be estimated from (Chen et al., 2012) (see Appendix for details)

$$\frac{G}{E} = 2\xi_\alpha A_1 \frac{\cos\alpha \sin\omega}{l^2 \cos^2\omega}, \tag{27}$$

where ξ_α is a dimensionless parameter defined as

$$\xi_\alpha = \cos\alpha + \frac{12(EI)_1 \sin^2\alpha}{(EA)_1 l^2 \cos\alpha}. \tag{28}$$

Next, numerical simulations were performed to estimate the shear stiffness of the structures subjected to shearing loads. Each computational model consisted of three lattice unit cells in the longitudinal direction and seven lattice unit cells in the transverse directions, and were meshed using 20-node hexahedral elements. Table 1 shows the geometrical parameters of the lattices that were modeled. At least two elements were used along the thickness and width of the secondary corrugated core struts. All degrees of freedom of the bottom face sheet were set to zero while a longitudinal displacement was applied to the top face sheet to simulate the shearing load.

4.2. Strength

Following the analysis presented in Section 3.2, five competing failure modes were investigated for the "corrugated-pyramidal" 2nd order lattice truss structures under shear (see Appendix for details).

4.2.1. Face sheet wrinkling (FW) of the 2nd order lattice truss

As mentioned earlier, this failure mode is mainly caused by localized bulking of face sheets of the 1st order pyramidal truss between adjacent nodes. The critical load of buckling, F_f, is (see Appendix for details)

$$F_f = \frac{\pi^2 (EI)_1^f}{2\mu^2 {l_c}^2 \cos^2\omega_c}, \tag{29}$$

where $\mu = 0.5$, and the bending rigidity of the 1st order face sheets, $(EI)_1^f$, is

$$(EI)_1^f = \frac{E b_f {t_f}^3}{12}. \tag{30}$$

Furthermore, the relationship between the critical load of buckling, F_f, and the axial load along core I, F_A, is

$$F_A = (1 + \zeta_c) F_f, \tag{31}$$

where

$$\zeta_c = \frac{t_c^3 \sin^2\omega_c \cos\omega_c + t_c l_c^2 \cos^3\omega_c}{2 t_f l_c^2}. \tag{32}$$

Now, substituting Eq. (29) into Eq. (31) gives the axial load along core I as

$$F_A = \frac{(1 + \zeta_c)\pi^2 E b_f {t_f}^3}{6 {l_c}^2 \cos^2\omega_c}, \tag{33}$$

which can be used, along with the relationship between the axial load of core I and shearing load, to find the equivalent shear strength of the unit cell as (see Appendix for details)

$$\bar{\tau} = \frac{\xi_\alpha (1 + \zeta_c)\pi^2 E b_f {t_f}^3}{3 l^2 {l_c}^2 (\sin\varphi + \cos\varphi) cos^2\omega_c \cos^2\omega}. \tag{34}$$

4.2.2. Face sheet crushing (FC) of the 2nd order lattice truss

The failure load of the 1st order face sheets, F_f, is (see Appendix for details)

$$F_f = 2b_f t_f \sigma_f. \tag{35}$$

Now, by substituting Eq. (35) into Eq. (31), the axial load along core I is

$$F_A = 2(1+\zeta_c) b_f t_f \sigma_f, \tag{36}$$

which can further be used to obtain the equivalent shear strength of the unit cell with the following expression:

$$\bar{\tau} = \frac{4(1+\zeta_c)\xi_\alpha b_f t_f \sigma_f}{l^2(\sin\varphi + \cos\varphi)\cos^2\omega}. \tag{37}$$

4.2.3. Core member buckling (CE) of the 2nd order lattice truss

Similar to the analysis presented in Section 3, the critical axial load of buckling can be calculated by

$$F_c = \frac{\pi^2 (EI)_{\mathrm{II}}}{\mu^2 {l_c}^2}, \tag{38}$$

where $\mu = 0.5$. Then, the relationship between the axial load along core II, F_c, and in-plane compressive load, F_s, is

$$F_s = \lambda_c F_c, \tag{39}$$

where

$$\lambda_c = \cos\omega_c + \frac{t_c^2 \sin^2\omega_c}{l_c^2 \cos\omega_c} + \frac{2t_{\mathrm{f}}}{t_c \cos^2\omega_c}. \tag{40}$$

Then, closed-form expression of equivalent shear strength of the unit cell is

$$\bar{\tau} = \frac{2\lambda_c \xi_\alpha \pi^2 E b_f {t_c}^3}{3{l_c}^2 l^2 (\sin\varphi + \cos\varphi)\cos^2\omega}. \tag{41}$$

4.2.4. Core member crushing (CC) of the 2nd order lattice truss

The failure load of failure is

$$F_c = b_f t_c \sigma_f. \tag{42}$$

Similar to previous calculations, $F_A = \lambda_c F_c$, thus, the equivalent shear strength of the unit cell is

$$\bar{\tau} = \frac{2\lambda_c \xi_\alpha b_f t_c \sigma_f}{l^2(\sin\varphi + \cos\varphi)\cos^2\omega}. \tag{43}$$

4.2.5. Macro Euler buckling of the 1st order pyramidal truss

The critical load of failure, F_{cr}, is

$$F_{cr} = \frac{\pi^2 (EI)_{\mathrm{I}}}{\mu^2 l^2}, \tag{44}$$

where $\mu = 0.5$. Then, the equivalent shear strength of the unit cell is

$$\bar{\tau} = \frac{8\xi_\alpha \pi^2 (EI)_{\mathrm{I}}}{l^4(\sin\varphi + \cos\varphi)\cos^2\omega}. \tag{45}$$

5. In-plane compression of sandwich columns

Fig. 5 shows the possible modes of failure for the 2nd order lattice truss structures subjected to in-plane compression. Analytical expressions of failure force associated with each of these modes are discussed below.

5.1. Macro Euler buckling of the 1st order pyramidal truss

The critical load, F, associated with the macro Euler buckling of the 1st order pyramidal struts (shown in Fig. 5(a)) is (see Appendix for details)

$$F = \frac{\pi^2 (EI)_{eq}}{2n^2 \mu^2 l^2 \cos^2\omega}, \tag{46}$$

where $\mu = 0.5$, n is the number of the "corrugated-pyramidal' cells, and $(EI)_{eq}$ is the equivalent flexural rigidity of the 2nd order corrugated cell.

5.2. Face sheet wrinkling (FW) of the 1st order pyramidal truss

For this mode of failure, shown schematically in Fig. 5(b), the critical load is (see Appendix for details)

$$F_f = \frac{\pi^2 (EI)_f}{\mu^2 l^2 \cos^2\omega}, \tag{47}$$

where $\mu = 0.5$, and $(EI)_f = \sqrt{2} E l \cos\omega t^3$ is the flexural rigidity of the 1st order face sheets. We should note that part of the compressive load on the structure is carried by the "corrugated-pyramidal" lattice core due to its deformation under in-plane compressive loads. Thus, we can obtain the total in-plane compressive load as follow (see Appendix for details):

$$F = \frac{\sqrt{2}(1+\zeta_p)\pi^2 E t^3}{3l\cos\omega}, \tag{48}$$

where

$$\zeta_p = \frac{(EA)_{\mathrm{I}} \cos^3\beta}{2(EA)_f} + \frac{12(EI)_{\mathrm{I}} \sin^2\beta \cos\beta}{(EA)_f l^2}, \tag{49}$$

where the compressive stiffness of the 1st order face sheets is $(EA)_f = \sqrt{2} E l t \cos\omega$.

5.3. Face sheet crushing (FC) of the 1st order pyramidal truss

The failure load associated with face sheet crushing of the 1st order pyramidal truss (Fig. 5(c)) is

$$F_f = 2\sqrt{2}\sigma_f l t \cos\omega, \tag{50}$$

where σ_f is the average collapse strength of the 1st order face sheets, which can be directly measured from compression tests. Then the in-plane compressive load can be estimated from

$$F = 2\sqrt{2}(1+\zeta_p)\sigma_f l t \cos\omega. \tag{51}$$

5.4. Face sheet wrinkling (FW) of the 2nd order lattice truss

This mode of failure is characterized by localized buckling of the 2nd order face sheets between adjacent nodes, Fig. 5(d), where the critical in-plane compressive load is

$$F_f = \frac{\pi^2 (EI)_{\mathrm{I}}^f}{2\mu^2 {l_c}^2 \cos^2\omega}. \tag{52}$$

Note that the relationship between the critical in-plane load and axial load along core II is specified as

$$F_A = (1+\zeta_c) F_f. \tag{53}$$

Thus, the critical in-plane compressive load is

$$F = \frac{\lambda_p (1+\zeta_c)\pi^2 E b_f t_f^3}{6{l_c}^2 \cos^2\omega}, \tag{54}$$

where

$$\lambda_p = 2\cos\beta + \frac{(EA)_f}{(EA)_{\mathrm{I}} \cos^2\beta} + \frac{12(EI)_{\mathrm{I}} \sin^2\beta}{(EA)_{\mathrm{I}} l^2 \cos\beta}. \tag{55}$$

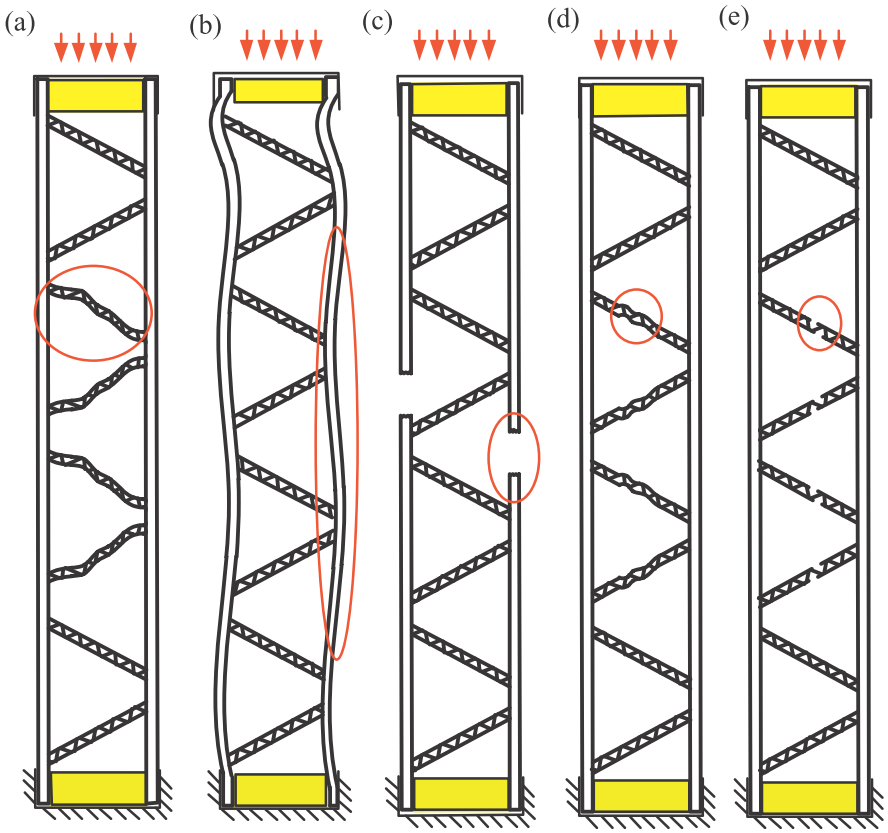

Fig. 5. Failure modes in the "corrugated-pyramidal" columns subjected to in-plane compression. (a) Macro Euler buckling of the 1st order pyramidal truss; (b) Face sheet wrinkling (FW) of the 1st order pyramidal truss; (c) Face sheet crushing (FC) of the 1st order pyramidal truss; (d) Face sheet wrinkling (FW) of the 2nd order lattice truss; (e) Face sheet crushing (FC) of the 2nd order lattice truss.

5.5. Face sheet crushing (FC) of the 2nd order lattice truss

The critical load associated with the 2nd order face sheet crushing (Fig. 5(e)) is

$$F_f = 2b_f t_f \sigma_f. \tag{56}$$

With reference to the method presented in Section 3.2, it can be used to obtain the following closed-form expression for critical in-plane compressive load associated with this mode of failure as

$$F = 2\lambda_p(1+\zeta_c)b_f t_f \sigma_f. \tag{57}$$

6. Three-point bending of sandwich beams

Here, we assume that the lattice core carries the internal shearing load, while the face sheets carry the internal bending moment during three-point bending. Fig. 6 shows four possible failure modes of sandwich panels including 1st order face sheet wrinkling, 1st order face sheet crushing, the Euler buckling of the 2nd order corrugated struts, and the macro Euler buckling of the 1st order pyramidal struts.

6.1. Face sheet wrinkling (FW) of the 1st order pyramidal truss

Due to geometrical characteristics of the structures, imposed constraints, and external loads with axially symmetric distributions, the modes of failure can be analyzed by considering half of the structure. Then, the bending moment at the middle section of the structure is (see Appendix for details)

$$M = \frac{\sqrt{2}}{4} nFl\cos\omega, \tag{58}$$

where n denotes the number of the 1st order unit cells, and F is the applied external load on the middle section. We should note that there is no "corrugated-pyramidal" lattice core at the midsection where the load is applied. Therefore, the face sheet carries most of the applied load. The in-plane load of the 1st order face sheets is

$$F_f = \frac{\sqrt{2}\cos\omega}{4\sin\omega} nF. \tag{59}$$

The critical load associated with the face sheet wrinkling between two adjacent nodes can be estimated as

$$F_f = \frac{\pi^2 (EI)_f}{2\mu^2 l^2 \cos^2\omega}, \tag{60}$$

where $\mu = 0.5$. Thus, the external load is

$$F = \frac{4\sqrt{2}\pi^2 (EI)_f \sin\omega}{nl^2\cos^3\omega}. \tag{61}$$

6.2. Face sheet crushing (FC) of the 1st order pyramidal truss

The critical load of crushing is

$$F_f = \sqrt{2}\sigma_f lt\cos\omega, \tag{62}$$

where σ_f denotes the average strength of the parent material. Then, based on the relation between the critical load of collapse of the face sheets, F_f, and the applied load, F, in Eq. (59), we can obtain F with the following expression:

$$F = \frac{4}{n}\sin\omega\sigma_f lt. \tag{63}$$

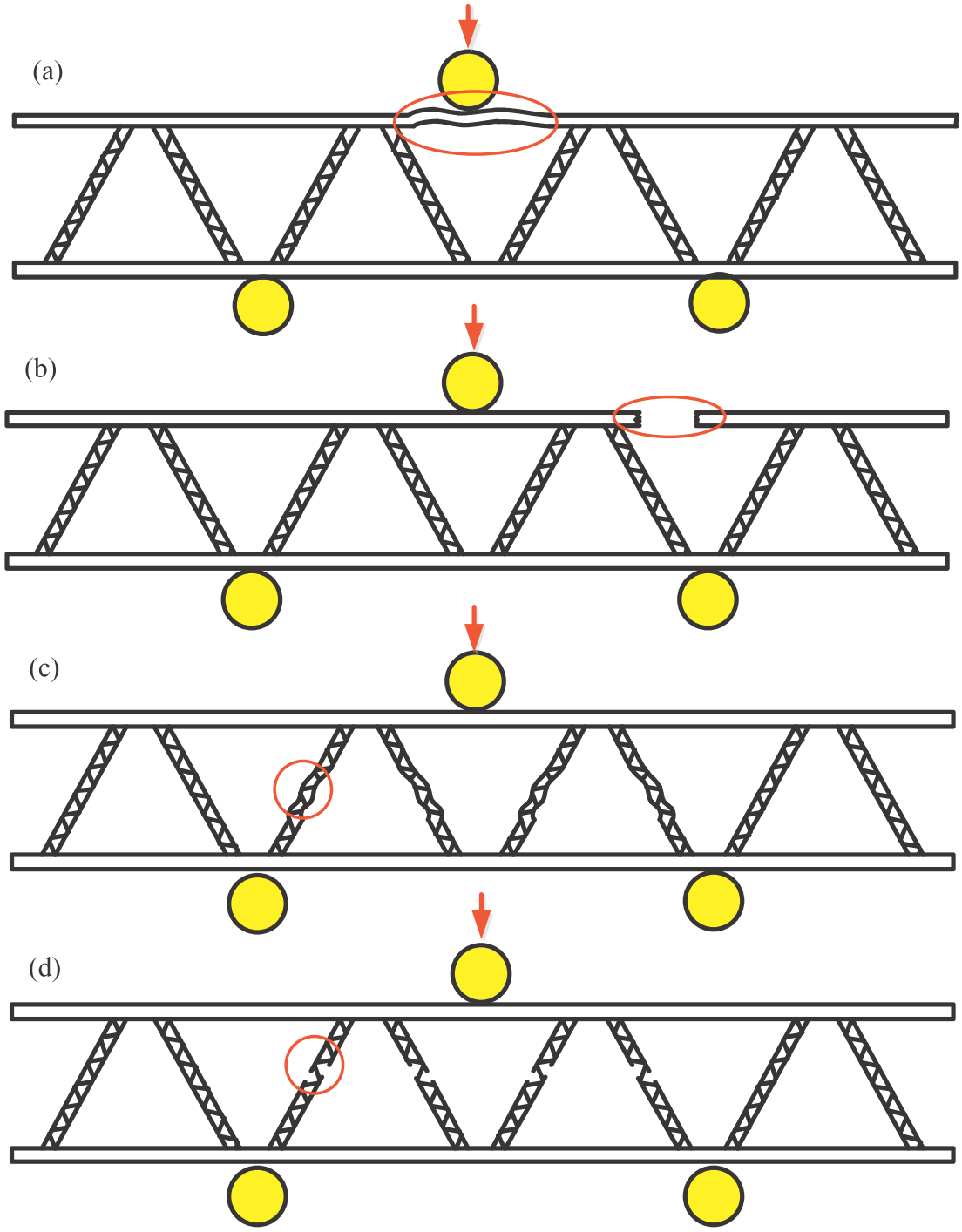

Fig. 6. The schematic diagram of failure modes under three-point bending: (a) Face sheet wrinkling (FW) of the 1st order pyramidal truss; (b) Face sheet crushing (FC) of the 1st order pyramidal truss; (c) Face sheet wrinkling (FW) of the 2nd order lattice truss; (d) Face sheet crushing (FC) of the 2nd order lattice truss.

6.3. Face sheet wrinkling (FW) of the 2nd order lattice truss

The critical load associated with this failure mode is

$$F = \frac{2\xi_\omega(1+\zeta_c)\pi^2 E b_f {t_f}^3}{3{l_c}^2\cos^2\omega_c}. \tag{64}$$

6.4. Face sheet crushing (FC) of the 2nd order lattice truss

The critical load associated with this failure mode is

$$F = 8\xi_\omega(1+\zeta_c)b_f t_f \sigma_f. \tag{65}$$

7. Results and discussion

7.1. Out-of-plane compression

Fig. 7 shows the failure map for sandwich panels with lattice cores subjected to out-of-plane compressive loads. In constructing this map that the angle between the core and face sheets for both the 1st and 2nd order lattice truss structures is assumed to be 45° (i.e., $\omega = \omega_c = 45°$). The results are presented in terms of non-dimensional parameters, t_f/l_c and t_c/l_c, for different values of the number of the 2nd order corrugated cells, n_1. Fig. 7(a) shows that

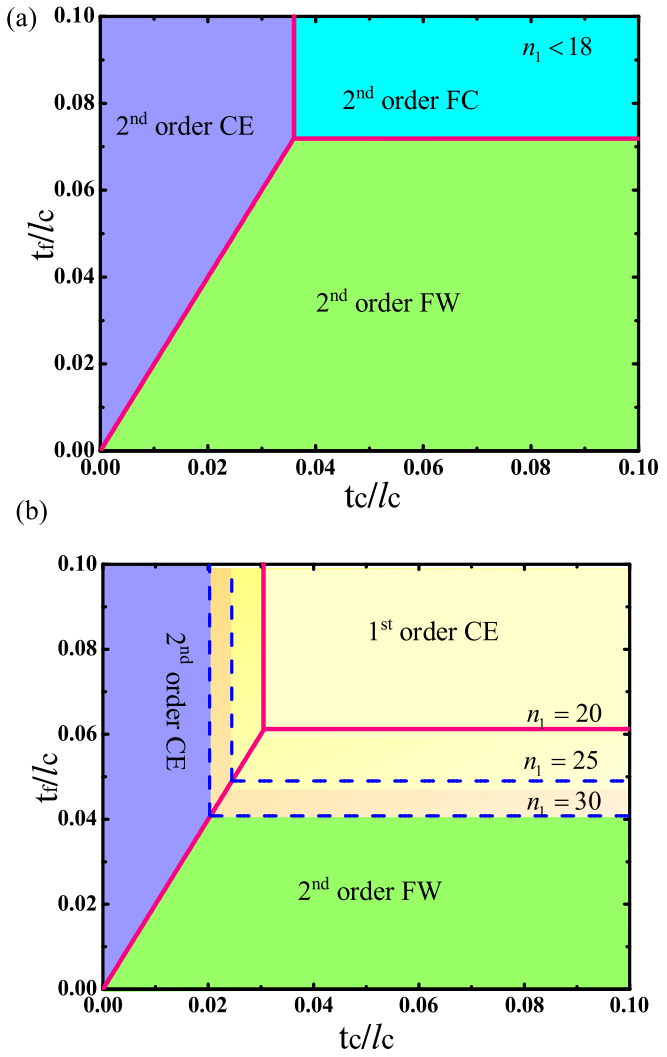

Fig. 7. Failure mechanism maps of the 2nd order lattice truss under out-of-plane compression with (a) the number of 2nd order corrugated cell, $n_1 < 18$ and (b) with the number of 2nd order corrugated cell, n_1=20, n_1=25 and n_1= 30 for three possible scenarios: FW = face sheet wrinkling; FC = face sheet crushing; CE = core member buckling.

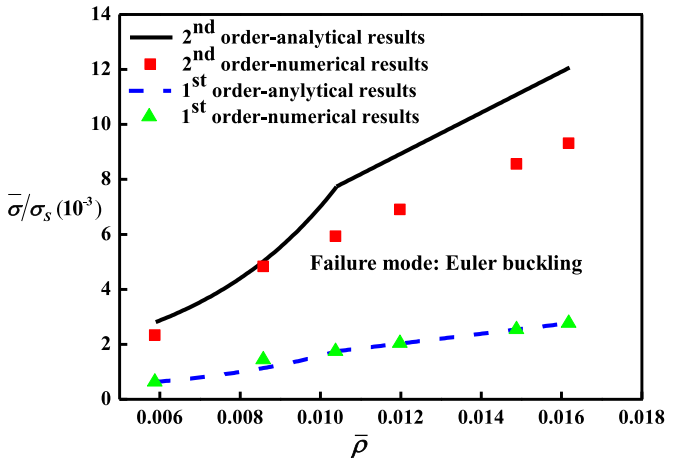

Fig. 8. Comparisons of compressive strength between the 2nd order lattice truss and the 1st order pyramidal truss with different relative densities.

the results are independent of the parameter, n_1, when it is smaller than 18. In this case, the dominant failure modes are: face sheet wrinkling (FW) and face sheet crushing (FC) of the 2nd order lattice truss, and Euler buckling of the 2nd order corrugated struts. Clearly, these three failure modes are independent of the length of the 1st order pyramidal core. The macro Euler buckling (CE) occurs when the parameter, n_1, is greater than 18 as shown in Fig. 7(b). This is mainly because the length of pyramidal struts becomes longer as the number of the 2nd order corrugated cells increases, resulting in a reduced buckling strength of 2nd order lattice truss. Furthermore, it can be seen that the macro Euler buckling of the 1st order pyramidal struts is more prone to occur at higher values of n_1. This observation is due to the fact that the structure becomes more prone to instability as the length of the pyramidal core increases.

A limited set of computational studies were performed to validate the results from our analytical investigations (see Section 3.1 for details). Table 2 lists the geometrical characteristics of six different samples we constructed in ABAQUS for compressive strength calculations. Note that material properties of the parent material are consistent with those in Table 1. Fig. 8 compares analytical and numerical results for compressive strength of 1st and 2nd order lattice trusses with different relative densities. Results show that the 2nd order lattice truss structure is much stronger compared to its 1st order counterpart with the same relative density due to its greater capacity in resisting buckling. The main reasons for discrepancies between theoretical and simulation results are, (1) the 2nd order lattice core is modeled as thin-walled cantilever structures with uniform cross sections in the analytical study. In addition, the cross-sectional moment of inertia is estimated by considering only the face sheets. Finally, the influence of discrete distribution of the 2nd order lattice core is neglected. (2) The influence of shear deformation is not taken into account for beam elements (i.e., Euler Bernoulli beam assumption). As the matter of fact, the thickness of the 2nd order corrugated struts are greater than the core rods in the 1st order pyramidal truss, thus, the shear deformation obviously affects the accuracy of the analytical expressions. At small relative core densities, the compressive strength of the 2nd order structures is almost four times greater than its 1st order counterpart with equal mass f. This is consistent with previous studies (Kooistra et al., 2007; Zhao et al., 2012; Zheng et al., 2016) with different types of hierarchical constructions.

Fig. 9 shows the failure mechanism map for out-of-plane compression constructed based on the analytical expressions presented in Section 3. The dots in this figure show the results from the experiments. Fig. 10(a) and (b) show images of specimens with two apparent failure modes: face sheet wrinkling of the 2nd order lattice truss and the mixed failure mode, in which the dominant failure mode is the core member buckling of the 2nd order lattice truss (note that the samples were painted by black color in these images to improve image quality). The mixed failure mode is observed because, (1) for the selected geometrical parameters, point I (on Fig. 9) is very close to the intersection of two failure modes; and (2) the material defects imposed in the fabrication process. Although the failure mechanism maps are dependent on the properties of the parent material, the analytical closed-form expressions presented for elastic modulus and strength of the hierarchical lattice structures are independent on the parent material as long as the parent material is linear elastic and reaches plasticity at some point. The compressive stress-strain responses of these specimens are given in Fig. 10(c), which start with a linear elastic regime until a peak value, followed by a nonlinear regime due to the progressive failure of the truss members. The analytical results associated with the failure of two specimens can be calculated by Eqs. (14) and (22) as 0.039 MPa and 0.084 MPa. Compared with the experimental results of 0.032 Ma and 0.069 MPa, respectively, the

Table 2
Dimensions of the six different specimens for compressive strength simulations.

Structural topologies	Relative density (%) ($\bar{\rho}$)	Truss-I (mm) ($l \times b_f \times t_f$)	Truss-II (mm) ($l_c \times t_c$)
1st order	0.59	111.12 × 5.71 × 2.85	/
2nd order		111.12 × 5.71 × 1.43	2.86 × 0.14
1st order	0.86	77.78 × 5 × 2.45	/
2nd order		77.78 × 5 × 1.25	2.5 × 0.13
1st order	1.04	75 × 6.02 × 2.37	/
2nd order		75 × 6.02 × 1.2	2.41 × 0.12
1st order	1.2	622.25 × 60 × 19.73	/
2nd order		622.5 × 60 × 10	20 × 1
1st order	1.49	51.85 × 6.67 × 1.65	/
2nd order		51.85 × 6.67 × 0.83	1.67 × 0.083
1st order	1.62	207.42 × 30 × 6.61	/
2nd order		207.42 × 30 × 3.33	6.67 × 0.33

Table 3
Dimensions of the three different hierarchical specimens under out-of-plane compression.

Failure modes	Truss-I (mm) ($l \times b_f \times t_f$)	Truss-II (mm) ($l_c \times t_c$)
Face sheet wrinkling of the 2nd order lattice truss	83.14 × 10 × 0.8	11.48 × 1.5
Mixed failure modes	83.14 × 10 × 1.5	13.38 × 0.8

The mixed failure modes include core member buckling of 2nd order lattice truss and face sheet wrinkling of 2nd order lattice truss.

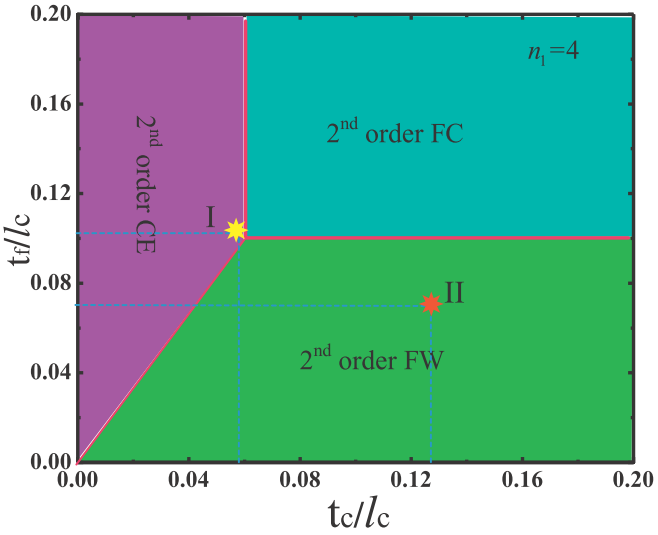

Fig. 9. Failure mechanism maps of the 2nd order lattice truss made with 3D printing material under out-of-plane compression: FW = face sheet wrinkling; CE = core member buckling and the experimental points I and II locate in two different failure modes, respectively.

theoretical compressive strength of the hierarchical structures is approximately 20.2% and 23.5% higher. This is associated with fabrication defects that can be introduced during the manufacturing process. The failure modes observed in experiments are consistent with the dominant failure mode as predicted by the theory.

Moreover, previous studies (Kenny, 1996; Deshpande and Fleck, 2000) show that the strain rate (in the range of 10^{-3}–10^{3} s^{-1}) has little effect on energy absorption and overall dynamic behavior of foams and cellular materials. We can show that our static analysis can be easily extended to dynamic regimes to estimate the energy absorption properties of hierarchical lattice structures.

7.2. Shear

Fig. 11 plots the equivalent shear stiffness of the 1st and 2nd order lattice truss structures versus relative density, where the dashed and solid lines show the analytical results and the markers show the simulation results. The equivalent shear stiffness is normalized by the Young's modulus of the parent material. Results reveal that the equivalent shear stiffness of the "corrugated-pyramidal" 2nd order lattice truss structures is slightly lower than its 1st order counterpart. Similar to the compressive stiffness (shown in Fig. 2), this is mainly due to the fact that in contrast to the 1st order pyramidal truss structures at which all the members contribute almost equally to the overall shear stiffness of the structures, for the 2nd order lattice truss structures with the "corrugated-pyramidal" lattice cores, greater part of the load is carried by the 2nd order face sheets and the contribution of corrugated struts is negligible. Thus, the equivalent shear stiffness of the 2nd order lattice truss structures is slightly lower than its 1st order counterpart of equal mass.

Fig. 12 presents the equivalent shear strength normalized by the strength of the parent material versus relative density for both 1st and 2nd order lattice truss structures. The results show that the 2nd structures are much stronger compared to the 1st order pyramidal truss structures in terms of its shear strength. This is mainly due to a higher "anti-buckling" capacity (i.e., superior ability to resist buckling) of the 2nd order structures, where their bending stiffness is significantly greater than the 1st order pyramidal core of equal mass. This suggests that the 2nd order corrugated core can fully exploit the load-bearing capacity of the material compared to its 1st order counterpart.

7.3. In-plane compression

The analytical expressions derived in Section 5 are employed to construct two-dimensional collapse mechanism maps under in-plane compression, Fig. 13. The results are plotted as functions of non-dimensional parameters, t/l and t_f/l_c, for both the 1st and 2nd order lattice truss structures with $\omega = \omega_1 = 45^\circ$. Moreover, parameters n and n_1 are defined as the number of the 1st order pyramidal unit cells and the number of the 2nd order corrugated unit cells, respectively. We should note that due to the geometry of these structures and nature of the applied load, most of the in-plane compressive load is carried by the 1st order face sheets. In other words, the 2nd order corrugated core does not make a considerable contribution to the load-bearing capacity of the structure under in-plane compression, thus the failure modes associated with 2nd order structure are not likely to occur within the structures. Furthermore, a localized collapse of corrugated struts has negligible

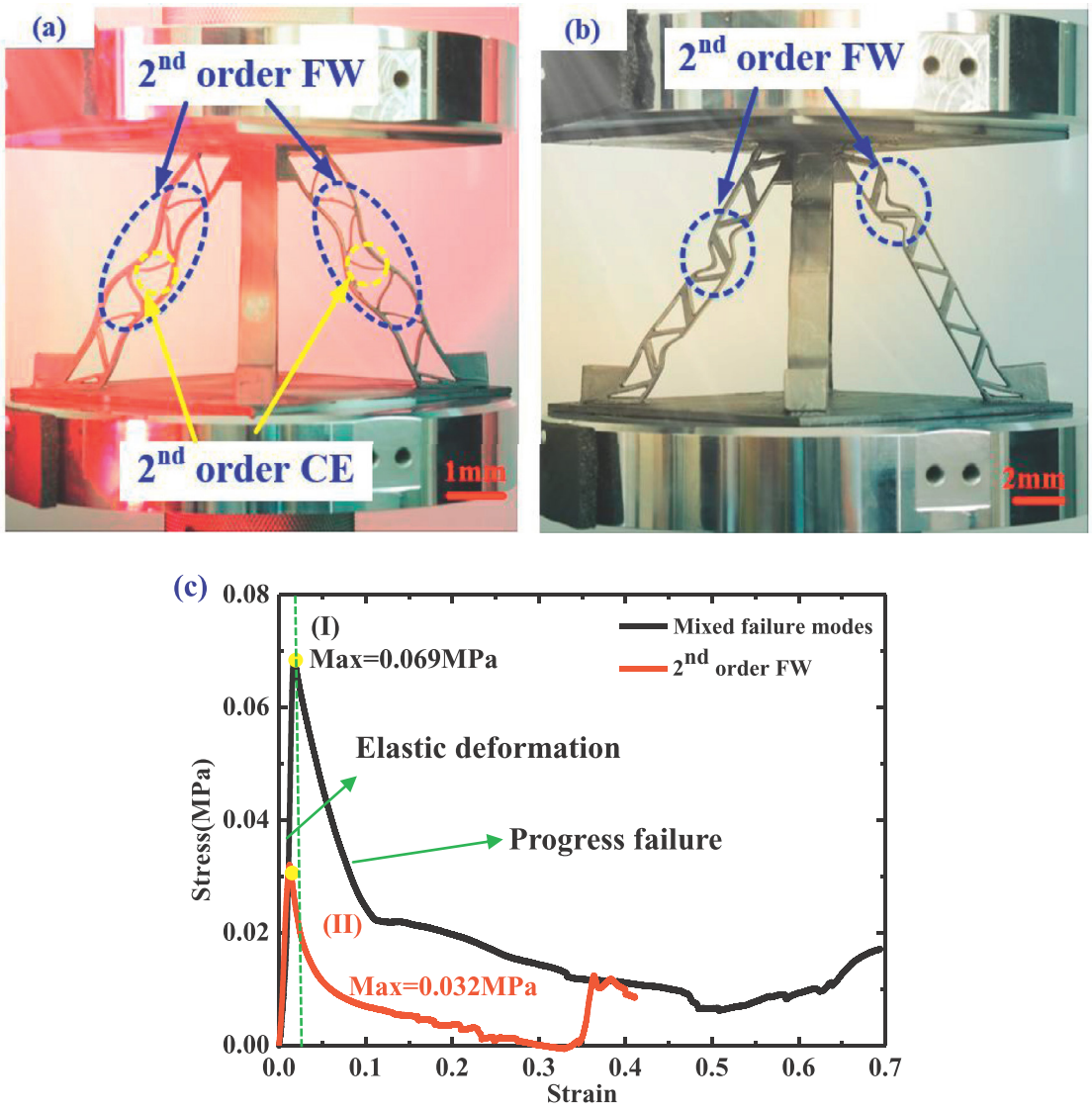

Fig. 10. (a) The mixed failure modes including core member buckling (CE) of the 2nd order lattice truss and face sheet wrinkling (FW) of the 2nd order lattice truss; (b) Face sheet wrinkling (FW) of the 2nd order lattice truss; (c) Compression stress-strain curves for two different failure modes: (I) the mixed failure modes including core member buckling (CE) of the 2nd order lattice truss and face sheet wrinkling (FW) of the 2nd order lattice truss; (II) face sheet wrinkling (FW) of the 2nd order lattice truss.

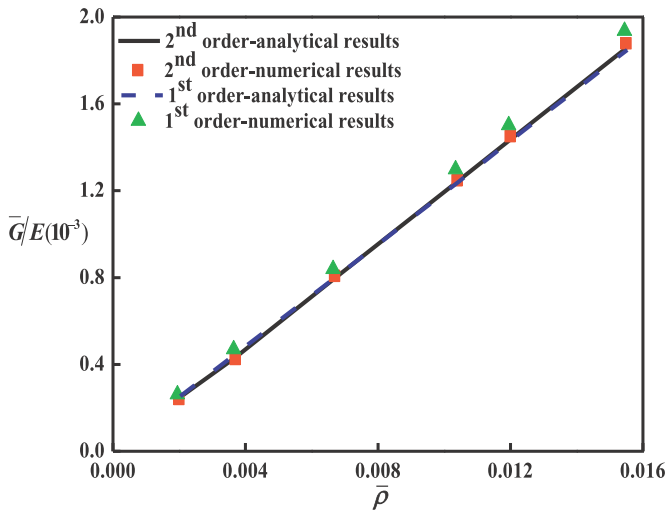

Fig. 11. Comparisons of shear stiffness between the 2nd order lattice truss and the 1st order pyramidal truss with different relative densities. .

effect on the load-bearing capacity of the structure, and is ignored in this study. To understand the effect of the 2nd order corrugated struts on the overall flexural rigidity of these structures, we define a new parameter representing a non-identical thickness between the 2nd order face sheets and corrugated struts: $t_f = mt_c$. The results for $n = 8$, $n_1 = 4$, and $m = 2$ are shown in Fig. 13(a).

Our calculations show that the parameters, n_1 and m, have almost no effect on the failure modes shown in Fig. 13(a), when n is smaller than 20. This is because the length of 2nd order corrugated core struts has no effect on the structural failure modes. Thus, in this case the failure of corrugated cores can be neglected. Results show that the face sheet wrinkling (FW) of the 2nd order lattice truss is the most dominant failure mode at small core relative densities due to the lower thickness of the face sheets (i.e., lower critical load of buckling). In contrast, face sheet crushing (FC) of the 2nd order lattice truss becomes the most dominant mode of failure at higher relative densities. Moreover, the macro Euler buckling of the 1st order pyramidal struts occurs when n becomes greater than 20. Fig. 13(b) presents a collapse mechanism map for structures with $n = 30$, and $m = 2$, where the value of n_1 is set to $n_1 = 2$, and $n_1 = 4$. The results confirm that the

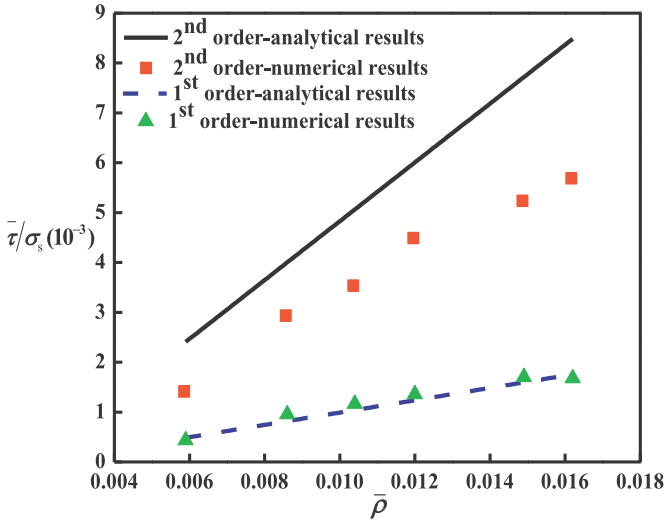

Fig. 12. Comparisons of the shear strength between the 2nd order lattice truss and the 1st order pyramidal truss with different relative densities.

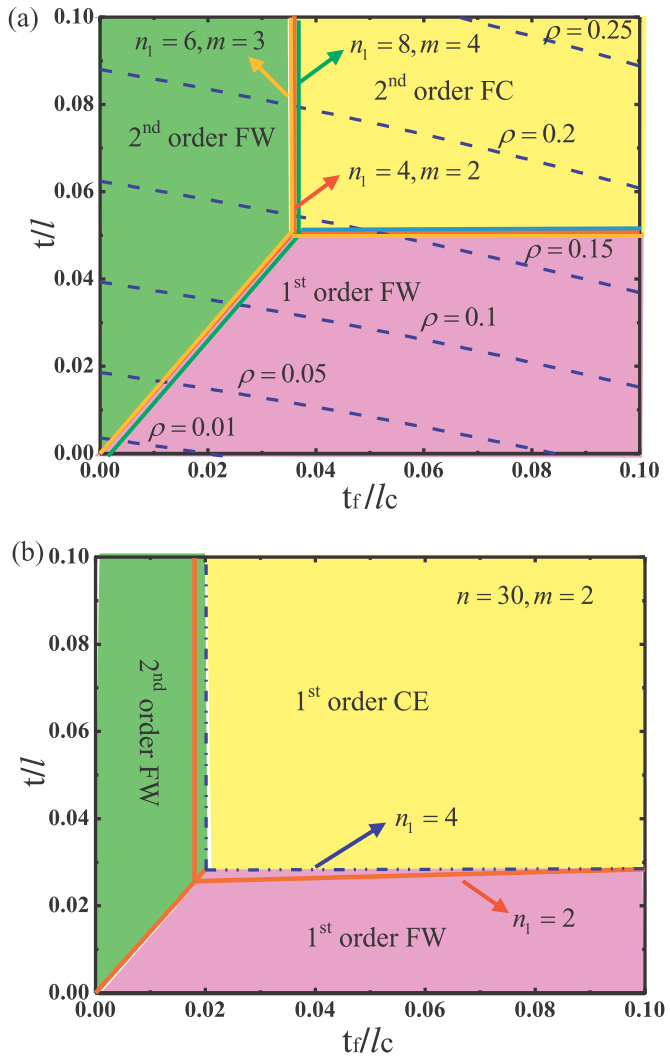

Fig. 13. Failure mechanism maps of the 2nd order lattice truss under in-plane compression with (a) the number of the 1st order pyramidal cell, $n < 20$, and (b) with the number of the 2nd order corrugated cell, $n = 30$, $n_1 = 2$, $m = 2$ and $n = 30$, $n_1 = 4$, $m = 2$ for two possible scenarios: FW = face sheet wrinkling; FC = face sheet crushing; CE = core member buckling.

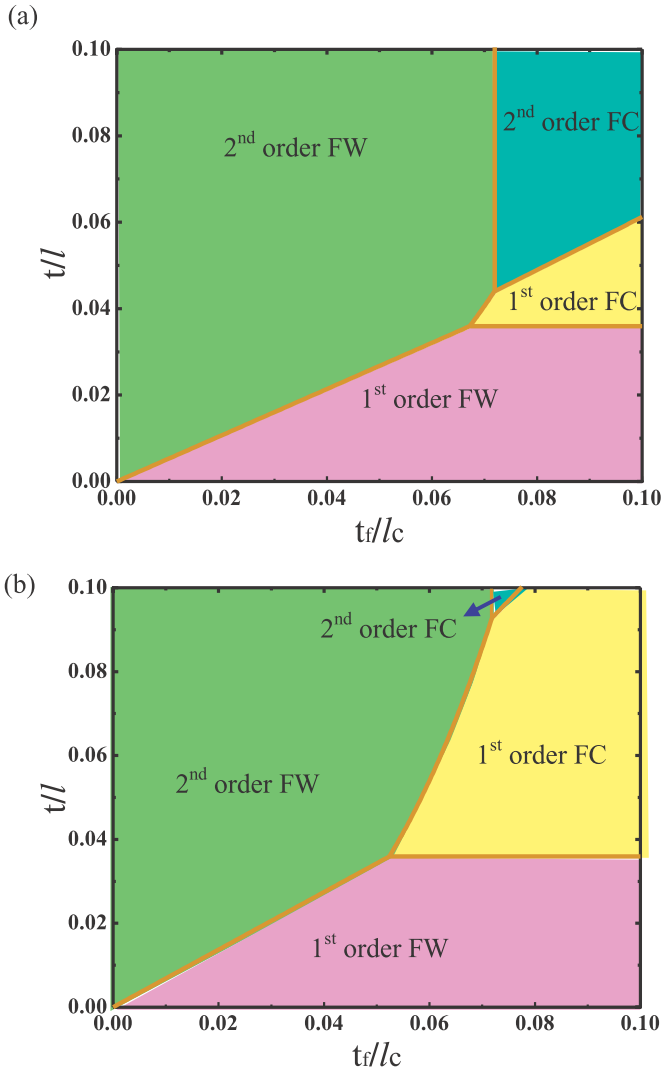

Fig. 14. Failure mechanism maps of the 2nd order lattice truss with invariable length of sandwich strut under three-point bending: FW = face sheet wrinkling; FC = face sheet crushing and (a) $n = 9$, $n_1 = 4$; (b) $n = 19$, $n_1 = 4$.

macro Euler buckling is less likely to happen as the number of 2nd order corrugated unit cells increases (i.e., greater n_1). We should note that the length of the 2nd order corrugated cores directly affect the distance between the 2nd order face sheets, which further affects the buckling resistance of the structure (i.e., higher buckling resistance with longer distance between the two face sheets). The hierarchy suppresses the macro Euler buckling failure mode in this structure even in structures with $n_1 = 2$. Therefore, increasing the length of the 2nd order corrugated truss member has no obvious effect on the ability of the structure to resist buckling. Besides, the 2nd order corrugated struts make minimal contribution to the flexural rigidity of the 2nd order truss core, and thus the parameter m has little influence on the transitions between different failure modes as shown in Fig. 13(b).

7.4. Three-point bending

The analytical relations presented in Section 6 are used to construct two-dimensional collapse mechanism maps for the structures under three-point bending loads. The results are plotted as functions of the normalized parameters, t/l and t_f/l_c, with $\omega = \omega_1 = 45°$, Fig. 14. Two sets of geometrical configurations were considered with $n = 9$ and $n_1 = 4$, and, $n = 19$ and $n_1 = 4$, Fig. 14(a)

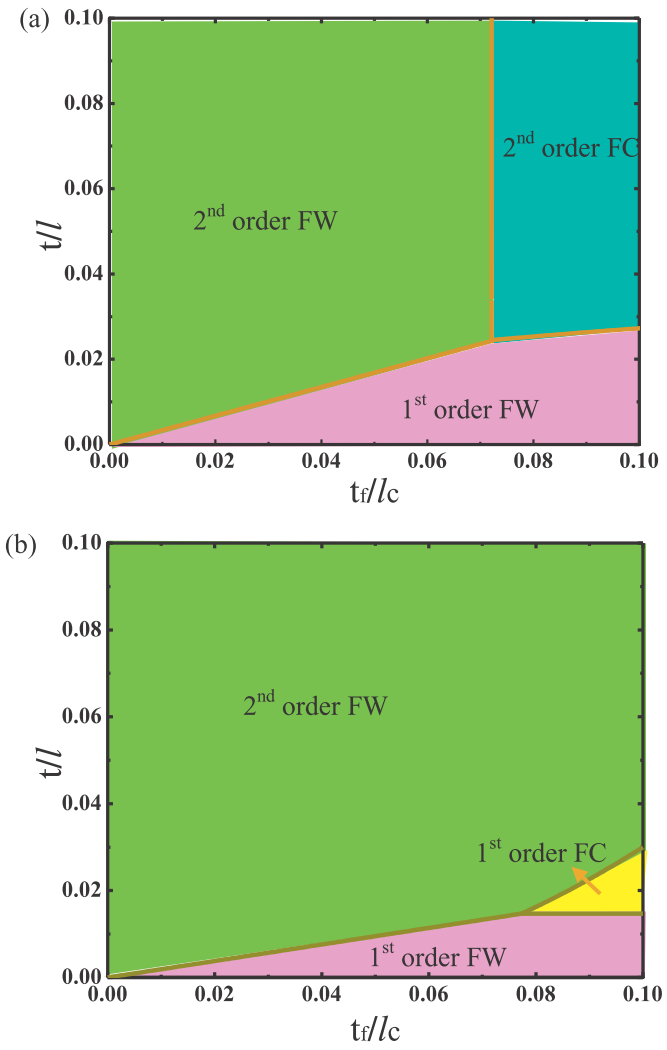

Fig. 15. Failure mechanism maps of the 2nd order lattice truss with invariable span under three-point bending: FW = face sheet wrinkling; FC = face sheet crushing and (a) $n = 9$, $n_1 = 4$; (b) $n = 19$, $n_1 = 4$.

and (b). Similar to the case of in-plane compressive loading, the localized buckling of corrugated struts has almost no effect on the load-bearing capacity of the structures, and therefore, can be ignored from our analysis. Furthermore, as mentioned earlier, the macro Euler buckling of the 1st order pyramidal struts will occur when n is greater than 20, thus, can be ignored as well.

Fig. 14 shows that by increasing parameter n, the area associated with the wrinkling of the 2nd order face sheets gradually decreases, while the area associated with the 2nd order face sheet crushing decreases rapidly. Face sheet crushing will not appear for structures with $n > 20$, which implies that this failure mode is not likely to occur in panels with low density core constructions. However, face sheet wrinkling and face sheet crushing of the 1st order pyramidal truss are more likely to occur. This is mainly because the span of the entire structure becomes larger with an increase in n, and thus, the midsection of the structure will carry a greater bending moment. Therefore, the face sheets will carry a greater in-plane load and the risk of face failure will increase drastically. Now we plot the failure mechanism maps for two cases with $n = 9$ and $n_1 = 2$, $n = 9$ and $n_1 = 8$, Fig. 15. The results show that the parameter n_1 has a major role in the transition of different failure modes. In the case of a constant bending moment, when n_1 is small, the in-plane load of face sheet increases, resulting in the face sheet becoming prone to damage and failure. However, the distance between top and bottom face sheets becomes greater with an increase in the parameter, n_1, which leads to a decrease in the in-plane load of face sheets. Thus, the corresponding failure modes are less likely to occur.

8. Conclusions

In the present paper, we investigated the mechanical response and failure of the "corrugated-pyramidal" 2nd order lattice truss structures under different quasi-static loading conditions. Analytical expressions of different failure modes have been derived under four types of static loadings: out-of-plane compression, shear, in-plane compression, and three-point bending. The relevant FE simulations were conducted to verify the validity of these analytical solutions, and good correlations between analytical predictions and FE simulations were achieved. In addition, a limited number of experiments were performed in order to further validate the analytical expressions related to each failure mode. The failure mechanism maps were constructed based on the analytical expressions for out-of-plane compressive, shear, in-plane compressive, and three-point bending strengths in each of these modes in order to investigate the influence of geometrical characteristics of on the mechanical response and failure of 2nd order lattice truss structures and sandwich panels.

Acknowledgements

The present work was supported in part by the National Science Foundation of China under grant Nos. 11302060, 11432004 and 11421091. J.X. also gratefully acknowledges supported by Program for Outstanding Young Scholars in Harbin Institute of Technology, the Science and Technology on Advanced Composites in Special Environment Laboratory and Young Elite Scientist Sponsorship Program by CAST no. YESS20160190. The work was supported in part by NSF Grant no. CMMI-1634560. D.V. and A.V. acknowledge the support by the United States National Science Foundation through grant award NSF-CMMI # 1634560.

Appendix

1. Equivalent out-of-plane compressive stiffness

Because the rods of the 1st order pyramidal lattice core have an axially symmetric distribution, the relevant effective stiffness of the lattice core can be derived by analyzing the deformation of a single strut. According to the geometric relationship between the vertical displacement and the axial, tangential displacement components of the rod, the corresponding expressions are

$$\delta_A = \delta \cos\alpha, \tag{A-1}$$

$$\delta_S = \delta \sin\alpha. \tag{A-2}$$

The axial displacement component δ_A is generated by the axial force F_A, from the basic mechanics of materials formulas and Eq. (A-1), the axial force is

$$F_A = \frac{(EA)_1}{l}\delta\cos\alpha. \tag{A-3}$$

The tangential displacement component δ_S is generated by shear force F_S and bending moment M, the tangential displacement also has following expression:

$$\delta_S = \frac{F_S l^3}{3(EI)_1} - \frac{Ml^2}{2(EI)_1}. \tag{A-4}$$

We assume clamped boundary conditions at the tips of core rods. The sum of rotation angles, which are produced by shear force F_S and bending moment M, at each end of the rod equal to zero. By equilibrium equations, the equation is

$$\frac{F_S l^2}{2(EI)_{\mathrm{I}}} - \frac{Ml}{(EI)_{\mathrm{I}}} = 0. \tag{A-5}$$

Substituting Eqs. (A-2) and (A-4) into Eq. (A-5), the shear force F_s and bending moment M can be further simplified as

$$F_S = \frac{12(EI)_{\mathrm{I}}}{l^3}\delta \sin\alpha, \tag{A-6}$$

$$M = \frac{6(EI)_{\mathrm{I}}}{l^2}\delta \sin\alpha. \tag{A-7}$$

The resultant force F along the vertical direction is

$$F = F_A \sin\omega + F_S \cos\omega. \tag{A-8}$$

Substituting Eqs. (A-3) and (A-6) into Eq. (A-8), the resultant force F can be further simplified as

$$F = \frac{(EA)_{\mathrm{I}} l^2 \sin^2\omega + 12(EI)_{\mathrm{I}} \cos^2\omega}{l^3}\delta. \tag{A-9}$$

The equivalent stress, $\bar{\sigma}$, of cellular sandwich structure is

$$\bar{\sigma} = \frac{2\xi_\omega (EA)_{\mathrm{I}} \sin\omega}{l^3 \cos^2\omega}\delta. \tag{A-10}$$

The dimensionless parameter, ξ_ω, in Eq. (A-10) is

$$\xi_\omega = \frac{(EA)_{\mathrm{I}} l^2 \sin^2\omega + 12(EI)_{\mathrm{I}} \cos^2\omega}{(EA)_{\mathrm{I}} l^2 \sin\omega}. \tag{A-11}$$

The equivalent strain, $\bar{\varepsilon}$, along the vertical direction (z-axis) of the unit cell is

$$\bar{\varepsilon} = \frac{\delta}{l \sin\omega}. \tag{A-12}$$

Thus, the equivalent out-of-plane compressive stiffness, $\bar{E}$, along the z-axis of the unit cell is

$$\bar{E} = \frac{2\xi_\omega (EA)_{\mathrm{I}} \sin^2\omega}{l^2 \cos^2\omega}. \tag{A-13}$$

We take a corrugated unit cell as the object of free-body-diagram as shown in Fig. A-1. The external force, F, is applied along the x-axis, then a half of a corrugated unit cell is taken as the object of free-body-diagram due to the symmetry of the structure. In addition, the displacement, δ, is generated along the direction of this external force. Under the premise of small deformations, the contribution of the axial deformation, which is generated by the surface force in the corrugated core, and the shear deformation, which is caused by the shear force and bending moment, to the displacement, δ, is considered. The response of the structure is investigated based on continuous displacements and equilibrium formulation. According to the geometric relationship of the displacement, the axial and shear displacement components, δ_A, and, δ_S, are

$$\delta_A = \delta \cos\omega, \tag{A-14}$$

$$\delta_S = \delta \sin\omega. \tag{A-15}$$

The axial displacement component, δ_A, is generated by the surface internal force, F_A, in the corrugated core. From basic mechanics of materials formulas and Eq. (A-14), the axial force, F_A, is

$$F_A = \frac{(EA)_{\mathrm{II}}}{l}\delta \cos\omega, \tag{A-16}$$

where the parameter $(EA)_{\mathrm{II}}$ denotes the equivalent compressive stiffness of the corrugated core.

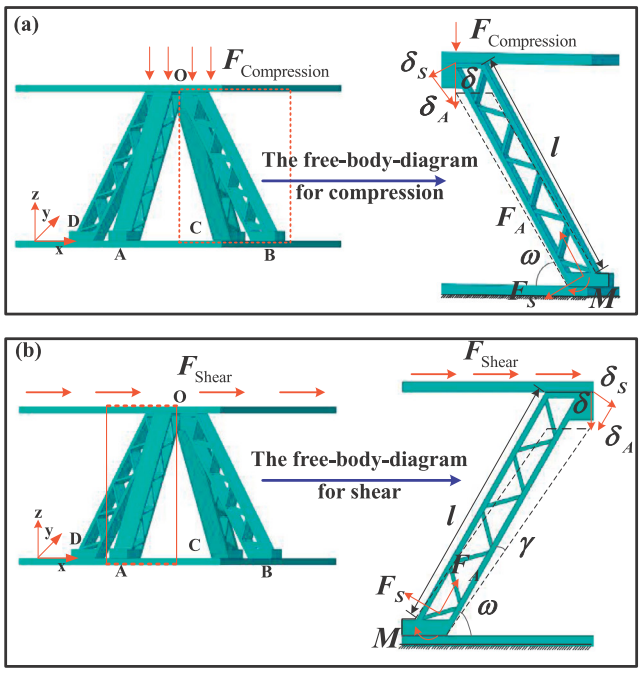

Fig. A-1. The free-body-diagram of a unit cell of 2nd order lattice truss and the corresponding schematic diagram of a quarter of a unit cell subjected to (a) compressive loading , and (b) shear loading.

Similarly, the shear deformation, δ_S, is caused by the shear force, F_S, and the bending moment, M, and the corresponding expression is

$$\delta_S = \frac{F_S l^3}{3(EI)_{\mathrm{II}}} - \frac{Ml^2}{2(EI)_{\mathrm{II}}}, \tag{A-17}$$

where the parameter $(EI)_{\mathrm{II}}$ denotes the equivalent flexural rigidity of the corrugated core.

We assume clamped boundary conditions at the tips of corrugated core. Likewise, the sum of the rotation angle equals to zero. By equilibrium equations, the equation is

$$\frac{F_S l^2}{2(EI)_{\mathrm{II}}} - \frac{Ml}{(EI)_{\mathrm{II}}} = 0. \tag{A-18}$$

Substituting Eqs. (A-15) and (A-17) into Eq. (A-18), the shear force, F_s, and the bending moment, M, of the corrugated core can be further simplified as

$$F_S = \frac{12(EI)_{\mathrm{II}}}{l^3}\delta \sin\omega, \tag{A-19}$$

$$M = \frac{6(EI)_{\mathrm{II}}}{l^2}\delta \sin\omega. \tag{A-20}$$

The infinitesimal displacement, δ, of the face sheet is generated by the component force, F_f, from basic mechanics of materials formulas, the component force along the face sheet is

$$F_f = \frac{(EA)_f}{l \cos\omega}\delta, \tag{A-21}$$

where the parameter $(EA)_f$ denotes the equivalent compressive stiffness of the face sheet.

The end force, F_r, of the right face sheet can be obtained based on the force equilibrium equations, and it is

$$F_r = F_A \cos\omega + F_S \sin\omega + F_f. \tag{A-22}$$

Substituting Eqs. (A-16) and (A-19) into Eq. (A-22), the end force of the right face sheet can be further simplified as

$$F_r = \left(\frac{(EA)_{\mathrm{II}} l^2 \cos^2\omega + 12(EI)_{\mathrm{II}} \sin^2\omega}{l^3} + \frac{(EA)_f}{l \cos\omega} \right)\delta. \tag{A-23}$$

The end force, F_l, of the left face sheet equals to that of the right face sheet, and the external, F, is the sum of the two end forces, that is

$$F = F_l + F_r. \tag{A-24}$$

Substituting Eqs. (A-21) and (A-23) into Eq. (A-24), the external force is

$$F = \frac{2(EA)_f}{l\cos\omega}\delta + \frac{(EA)_p l^2\cos^2\omega + 12(EI)_p\sin^2\omega}{l^3}\delta. \tag{A-25}$$

In Eq. (A-25), the first item denotes the load, F_f, which the top and bottom face sheets carry and the second item is the load, F_c, which the corrugated-pyramidal core carries. The ratio of F_f and F_c can be represented by a dimensionless parameter, ξ_c, and this parameter is defined as

$$\zeta_c = \frac{t_c^3\sin^2\omega\cos\omega + t_c l_c^2\cos^3\omega}{2t_f l_c^2}. \tag{A-26}$$

The equivalent strain, $\bar{\varepsilon}$, of the corrugated unit cell along the loading direction is

$$\bar{\varepsilon} = \frac{\delta}{2l_c\cos\omega}. \tag{A-27}$$

Thus the equivalent compressive stiffness of the corrugated unit cell along the loading direction is

$$(EA)_{\mathrm{I}} = \frac{F}{\bar{\varepsilon}}. \tag{A-28}$$

Substituting Eqs. (A-25) and (A-27) into Eq. (A-28), the equivalent compressive stiffness can be further simplified as

$$(EA)_{\mathrm{I}} = 2Ebt_f + \frac{Ebt_c^3\sin^2\omega\cos\omega}{l_c^2} + Ebt_c\cos^3\omega. \tag{A-29}$$

Similarly, the equivalent flexural rigidity of the corrugated unit cell is

$$(EI)_{\mathrm{I}} = \frac{1}{6}Ebt_f^3 + \frac{1}{2}\left(l_c\sin\omega + t_f\right)^2 Ebt_f + \frac{1}{4}\sin^2\omega\cos^3\omega l_c^2 Ebt_c + \frac{1}{12}f(\omega)Ebt_c^3, \tag{A-30}$$

where the parameter $f(\omega)$ is $f(\omega) = \cos\omega + 3\sin^2\omega\cos\omega - 3\sin^2\omega\cos^3\omega$.

2. Equivalent out-of-plane compressive strength

The compressive load, F, is applied along the z-axis and the relation between the axial force, F_A, and the compressive load, F, is

$$F = 4\xi_w F_A. \tag{A-31}$$

Then, the relations between the shear force, F_S, (the bending moment, M) and the axial force, F_A are

$$F_S = \frac{12(EI)_{\mathrm{I}}\cos\omega}{(EA)_{\mathrm{I}}l^2\sin\omega}F_A, \tag{A-32}$$

$$M = \frac{6(EI)_{\mathrm{I}}\cos\omega}{(EA)_{\mathrm{I}}l\sin\omega}F_A. \tag{A-33}$$

From Eqs. (A-32) and (A-33), it can be seen that the shear force and bending moment are far less than the axial force in the case of the truss member with larger aspect ratio. Thus, we can assume that the axial force is the dominant failure force of truss members under compressive load. The equivalent out-of-plane compressive strength, $\bar{\sigma}$ of a unit cell under the compressive load, F, is

$$\bar{\sigma} = \frac{F}{2l^2\cos^2\omega}. \tag{A-34}$$

2.1. Face sheet wrinkling (FW) of the 2nd order lattice truss

From the Section 3.2, the axial force along the 1st order pyramidal truss is

$$F_A = \frac{(1+\zeta_c)\pi^2 Eb_f {t_f}^3}{6{l_c}^2\cos^2\omega_c}. \tag{A-35}$$

Substituting Eqs. (A-31) and (A-35) into Eq. (A-34), the equivalent out-of-plane compressive strength, $\bar{\sigma}$, of a unit cell is

$$\bar{\sigma} = \frac{\xi_\omega(1+\zeta_c)\pi^2 Ebt_f^3}{3l^2{l_c}^2\cos^4\omega}. \tag{A-36}$$

2.2. Core member buckling (CE) of the 2nd order lattice truss

It can be assumed that the external load is slightly larger than the critical force of the strut, and the compressive strut is in the micro bending state. The actual stress state was estimated using the moment-equilibrium equations, and the relevant expression is

$$M(\mathrm{x}) = F_c w(x), \tag{A-37}$$

where $M(x)$ is the bending moment in the strut, and F_c denotes the external load along the attachment direction of the strut ends, and $w(x)$ is the deflection caused by external loads. In addition, according to the moment-equilibrium equations from basic mechanics of materials, the bending moment is

$$M(x) = -(EI)_{\mathrm{II}}\frac{d^2w}{dx^2}. \tag{A-38}$$

Substituting Eq. (A-38) into Eq. (A-37), the expression can be further simplified as

$$\frac{d^2w}{dx^2} + k^2w = 0, \tag{A-39}$$

$$k^2 = \frac{F_c}{(EI)_{\mathrm{II}}}. \tag{A-40}$$

According to the boundary conditions of compression strut, the minimum critical load of the stability problems of columns is

$$F_c = \frac{\pi^2(EI)_{\mathrm{II}}}{\mu^2{l_c}^2}. \tag{A-41}$$

3. Equivalent shear stiffness

The relation between the axial force, F_A, and the vertical displacement, δ, is

$$F_A = \frac{(EA)_{\mathrm{I}}}{l}\delta\cos\alpha. \tag{A-42}$$

In Eq. (A-9), $(EA)_{\mathrm{I}}$ and $(EI)_{\mathrm{I}}$ are the equivalent compressive stiffness and flexural rigidity of the 1st order core member respectively. According to the relation between the resultant force in Eq. (A-9) and the axial force in Eq. (A-42), the non-dimensional parameter, ξ_α, is defined as

$$\xi_\alpha = \frac{(EA)_{\mathrm{I}}l^2\cos^2\alpha + 12(EI)_{\mathrm{I}}\sin^2\alpha}{(EA)_{\mathrm{I}}l^2\cos\alpha}. \tag{A-43}$$

The relation between the resultant force and the axial force can be further simplified as

$$F = 4\xi_\alpha F_A. \tag{A-44}$$

The equivalent shear stress, $\bar{\tau}$, and equivalent shear strain, $\bar{\gamma}$, of a unit cell are

$$\bar{\tau} = \frac{2\xi_\alpha(EA)_{\mathrm{I}}\cos\alpha}{l^3\cos^2\omega}\delta, \tag{A-45}$$

$$\bar{\gamma} = \frac{\delta}{l \sin\omega}. \tag{A-46}$$

Thus, the equivalent shear stiffness, $\overline{G}$, of the unit cell is

$$\overline{G} = \frac{2\xi_\alpha (EA)_l \cos\alpha \sin\omega}{l^2 \cos^2\omega}. \tag{A-47}$$

4. Equivalent shear strength

The relations between the shear force, F_S, (the bending moment, M) and the axial force, F_A, through the free-body-diagram, the expression is

$$\frac{F_S}{F_A} = \frac{12(EI)_1 \sin\alpha}{l^2 (EA)_1 \cos\alpha}, \tag{A-48}$$

$$\frac{M}{F_A} = \frac{6(EI)_1 \sin\alpha}{l (EA)_1 \cos\alpha}. \tag{A-49}$$

It is seen from the Eqs. (A-48) and (A-49) that, the ratios of the shear force and the bending moment to the axial force can be sufficiently small provided that the 1st order pyramidal truss members are long enough. Thus, we can assume that the axial force is the dominant force to cause truss members damage under shear load. The shear load, F, can be along the random direction, therefore, the equivalent shear stiffness changes periodically with the angle. Since the truss members of the 1st order pyramidal unit cell are symmetrically positioned with respect to the central axis, one truss member rotates the angle, $\pi/2$, along this axis and this truss member will overlap the adjacent truss member. The angle of rotation is called the rotation angle. Here, the angle of rotation is $\pi/2$. The included angle, ϕ, between direction of shear load and x-axis is defined to $0 \le \phi < \pi/2$. The truss member named OC rod subjects to the maximum magnitude of compressive load and the other truss member named OA rod subjects to the maximum magnitude of tensile load as shown in Fig. A-1. The 2nd order lattice truss which is investigated is made of carbon fiber reinforced composite material and the compressive strength of the parent material is less than the tensile strength. Therefore, the truss member with the largest compressive load appears to damage primarily. Through the free-body-diagram, the relation between the axial force, F_A^{oc}, along the OC rod and shear force, F, is calculated by

$$F_A^{oc} = \frac{F}{4\xi_\alpha}(\sin\varphi + \cos\varphi). \tag{A-50}$$

Moreover, we also note that the analytical derivations of elastic modulus for the presented loading scenarios are not affected by the strength of the parent material, however, the theoretical calculations of failure strength will change if the compressive strength of the parent material is not less than the tensile strength. For this case, the tensile strength of the parent material can be substituted for the compressive strength in the analytical expressions. No matter what kind of loading is applied to the structure, the stretch-dominated truss members in "corrugated-pyramidal" hierarchical lattice cores will be subject to the tensile/compressive loads. Therefore, the tensile fracture of the hierarchical truss members is considered as the dominant failure mode on this occasion.

The OD rod begins to damage in the case of $\pi/2 \le \phi < \pi$ and the OA rod begins to damage in the case of $\pi \le \phi < 3\pi/2$, similarly, the OB rod begins to damage in the case of $3\pi/2 \le \phi < 2\pi$ due to the periodicity of the pyramidal sandwich structure.

The equivalent shear strength, $\overline{\tau}$, is

$$\bar{\tau} = \frac{2F_A\xi_\alpha}{l^2(\sin\varphi + \cos\varphi)\cos^2\omega}. \tag{A-51}$$

4.1. Face sheet wrinkling (FW) of the 2nd order lattice truss

Substituting Eqs. (31) and (32) into Eq. (A-51), the equivalent shear strength of a unit cell is

$$\bar{\tau} = \frac{\xi_\alpha(1+\zeta_c)\pi^2 E b_f {t_f}^3}{3{l^2}{l_c}^2(\sin\varphi + \cos\varphi)cos^2\omega_c\cos^2\omega}. \tag{A-52}$$

4.2. Face sheet crushing (FC) of the 2nd order lattice truss

Substituting the expression of the axial load along the core I (Eq. (36)) into Eq. (A-51), the equivalent shear strength of a unit cell is

$$\bar{\tau} = \frac{4(1+\zeta_c)\xi_\alpha b_f t_f \sigma_f}{l^2(\sin\varphi + \cos\varphi)\cos^2\omega}. \tag{A-53}$$

5. Equivalent in-plane compressive strength

5.1. Macro Euler buckling of the 1st order pyramidal truss

In Eq. (46), the expression of the equivalent flexural rigidity of the 2nd order corrugated cell is

$$(EI)_{eq} = 2(EI)_m + f_1(\beta,\theta)(EI)_1 + f_2(\beta,\theta)l^2(EA)_1, \tag{A-54}$$

where θ denotes the included angle between core I and axis 3. The non-dimensional parameters $f_1(\beta,\theta)$ and $f_2(\beta,\theta)$ are

$$f_1(\beta,\theta) = 4\cos\beta - 6\cos^2\beta\sin\theta + 3\cos^3\beta\sin^2\theta, \tag{A-55}$$

$$f_2(\beta,\theta) = \frac{1}{4}\cos^3\beta\cos^2\theta. \tag{A-56}$$

The expressions of the equivalent compressive stiffness and the equivalent flexural rigidity have been given in Eqs. (A-29) and (A-30). The equivalent flexural rigidity of the structural face sheets, the corresponding expression is

$$(EI)_m = \sqrt{2}Elt^3\cos\omega/12 + bt(l\sin\omega + t)^2/4. \tag{A-57}$$

5.2. Face sheet wrinkling (FW) of the 2nd order lattice truss

The distance between two adjacent nodes of the two face sheets is the same. Thus, the critical loads of the two face sheets under the buckling instability have the identical value. The total load which the two face sheets carry are the twice of that which a single face sheet carries. According to basic mechanics of materials formulas, the critical load is

$$F_f = \frac{\pi^2(EI)_{fm}}{\mu^2 l^2 \cos^2\omega}. \tag{A-58}$$

During the in-plane compression, the corrugated-pyramidal core may deform as the external load increases. Therefore, the cellular core will carry a partial load. The in-plane compressive load in this failure mode, through the free-body-diagram, is derived as

$$F = \frac{\sqrt{2}(1+\zeta_p)\pi^2 E t^3}{12\mu^2 l\cos\omega}. \tag{A-59}$$

In Eq. (A-59), the non-dimensional parameter, ζ_p, is

$$\zeta_p = \frac{(EA)_1\cos^3\beta}{(EA)_f} + \frac{12(EI)_1\sin^2\beta\cos\beta}{(EA)_f l^2}, \tag{A-60}$$

where the expressions of equivalent compressive stiffness and equivalent flexural rigidity of the 2nd order corrugated core have been given in Eqs. (A-29) and (A-30). The parameter, $(EA)_f$, indicates the equivalent compressive stiffness of the structural face sheets and $(EA)_f = \sqrt{2}Elt\cos\omega$.

6. Equivalent three-point bending strength

6.1. Face sheet wrinkling (FW) of the 1st order pyramidal truss

In Section 6, the external load of this failure mode has been obtained in Eq. (63), and the parameter $(EI)_f$ denotes the equivalent flexural rigidity of structural face sheet. It is

$$(EI)_f = \frac{\sqrt{2}lt^3\cos\omega}{12}. \tag{A-61}$$

Substituting Eqs. (A-61) and (60) into Eq. (59), the external load can be further calculated by

$$F = \frac{4\pi^2 t^3 E\sin\omega}{3nl\cos^2\omega}. \tag{A-62}$$

6.2. Face sheet wrinkling (FW) of the 2nd order lattice truss

The critical load associated with this failure mode is equal to the out-of-plane compressive strength of the 1st order FW (in Eq. (14)) multiply by the area of the 1st order unit cell. And the area of the 1st order unit cell is

$$A = 2l^2\cos^2\omega. \tag{A-63}$$

Therefore, the critical load is

$$F = \frac{2\xi_\omega(1+\zeta_c)\pi^2 E b_f {t_f}^3}{3{l_c}^2\cos^2\omega_c}. \tag{A-64}$$

6.3. Face sheet crushing (FC) of the 2nd order lattice truss

Similarly, the critical load under this failure mode is equivalent with the result which the out-of-plane compressive strength of the 1st order FC (in Eq. (17)) multiply by the area of the 1st order unit cell (in Eq. (A-63)). The corresponding expression is

$$F = 8\xi_\omega(1+\zeta_c)b_f t_f \sigma_f. \tag{A-65}$$

References

Ajdari, A., et al., 2008. Effect of defects on elastic–plastic behavior of cellular materials. Mater. Sci. Eng. A. 487 (1), 558–567.

Ajdari, A., Nayeb-Hashemi, H., Vaziri, A., 2011. Dynamic crushing and energy absorption of regular, irregular and functionally graded cellular structures. Int. J. Solids Struct. 48 (3-4), 506–516.

Ajdari, A., et al., 2012. Hierarchical honeycombs with tailorable properties. Int. J. Solids Struct. 49 (11), 1413–1419.

An, X., Fan, H., 2016. Hybrid design and energy absorption of luffa-sponge-like hierarchical cellular structures. Mater. Des. 106, 247–257.

Ashby, M.F., 2001. Drivers for material development in the 21st century. Prog. Mater. Sci. 46 (3), 191–199.

Barnett, D.M., Rawal, S., Rummel, K., 2001. Multifunctional structures for advanced spacecraft. J. Spacecraft Rockets. 38 (2), 226–230.

Chen, H., et al., 2012. Mechanical property of lattice truss material in sandwich panel including strut flexural deformation. Compos. Struct. 94 (12), 3448–3456.

Deshpande, A.S., Burgert, I., Paris, O., 2006. Hierarchically structured ceramics by high-precision nanoparticle casting of wood. Small 2 (8-9), 994–998.

Deshpande, V.S., Fleck, N.A., 2000. High strain rate compressive behaviour of aluminium alloy foams. Int. J. Impact Eng. 24 (3), 277–298.

Dong, L., Deshpande, V., Wadley, H., 2015. Mechanical response of Ti–6Al–4V octet-truss lattice structures. Int. J. Solids Struct. 60, 107–124.

Evans, A.G., 2001. Lightweight materials and structures. MRS Bull. 26 (10), 790–797.

Fan, H., et al., 2014. Designing and compression behaviors of ductile hierarchical pyramidal lattice composites. Mater. Des. 58, 363–367.

Han, S.C., Lee, J.W., Kang, K., 2015. A new type of low density material: shellular. Adv. Mater. 27 (37), 5506–5511.

Haghpanah, B., et al., 2014. Buckling of regular, chiral, and hierarchical honeycombs under a general macroscopic stress state. Proc. R. Soc. A. 470, 20130856.

Haghpanah, B., et al., 2013. Self-similar hierarchical honeycombs. Proc. R. Soc. A. 469 (2156), 5322–5334.

Hearn, E.J., 1997. Mechanics of Materials 2. Butterworth-Heinemann, Linacre House, Jordan Hill, Oxford, pp. 28–60.

Kazemahvazi, S., Dan, Z., 2009. Corrugated all-composite sandwich structures. Part 1: modeling. Compos. Sci. Technol. 69 (7), 913–919.

Kazemahvazi, S., Tanner, D., Dan, Z., 2009. Corrugated all-composite sandwich structures. Part 2: failure mechanisms and experimental programme. Compos. Sci. Technol. 69 (7), 920–925.

Kenny, L.D., 1996. Mechanical properties of particle stabilised aluminium foam. Mater. Sci. Forum. 217, 1883–1890.

Kooistra, G., Deshpande, V., Wadley, H., 2007. Hierarchical corrugated core sandwich panel concepts. J. Appl. Mech. 74 (2), 259–268.

Lakes, R., 1993. Materials with structural hierarchy. Nature 361 (6412), 511–515.

Liao, S., Zheng, Z., Yu, J., 2014. On the local nature of the strain field calculation method for measuring heterogeneous deformation of cellular materials. Int. J. Solids Struct. 51 (2), 478–490.

Lim, J.H., Kang, K.J., 2006. Mechanical behavior of sandwich panels with tetrahedral and Kagome truss cores fabricated from wires. Int. J. Solids Struct. 43 (17), 5228–5246.

Liu, T., Deng, Z.C., Lu, T.J., 2007. Minimum weights of pressurized hollow sandwich cylinders with ultralight cellular cores. Int. J. Solids Struct. 44 (10), 3231–3266.

Liu, J., et al., 2014. Experimental study on the low velocity impact responses of all-composite pyramidal truss core sandwich panel after high temperature exposure. Compos. Struct. 116, 670–681.

Liu, J., Xiang, L., Kan, T., 2015. The effect of temperature on the bending properties and failure mechanism of composite truss core sandwich structures. Compos. Part A 79, 146–154.

Mousanezhad, D., et al., 2015. Spiderweb honeycombs. Int. J. Solids Struct. 66, 218–227.

Mousanezhad, D., et al., 2016. Elastic properties of chiral, anti-chiral, and hierarchical honeycombs: a simple energy-based approach. Theor. Appl. Mech. Lett. 6 (2), 81–96.

Oftadeh, R., et al., 2014a. Mechanics of anisotropic hierarchical honeycombs. Int. J. Mech. Sci. 81, 126–136.

Oftadeh, R., et al., 2014b. Optimal fractal-like hierarchical honeycombs. Phys. Rev. Lett. 113 (10), 5880–5885.

Qiao, J., Chen, C., 2016. In-plane crushing of a hierarchical honeycomb. Int. J. Solids Struct. 85, 57–66.

Roper, C.S., 2011. Multiobjective optimization for design of multifunctional sandwich panel heat pipes with micro-architected truss cores. Int. J. Heat. Fluid. Fl. 32 (1), 239–248.

Schaedler, T.A., et al., 2011. Ultralight metallic microlattices. Science 334 (6058), 962–965.

Sun, F., Lai, C., Fan, H., 2016a. In-plane compression behavior and energy absorption of hierarchical triangular lattice structures. Mater. Des. 100, 280–290.

Sun, F., et al., 2016b. Crushing mechanism of hierarchical lattice structure. Mech. Mater. 97, 164–183.

Vaziri, A., Xue, Z., 2007. Mechanical behavior and constitutive modeling of metal cores. J. Mech. Mater. Struct. 2 (9), 1743–1761.

Wang, Z., Qin, Q., Zhang, J., Wang, T.J., 2013. Low-velocity impact response of geometrically asymmetric slender sandwich beams with metal foam core. Compos. Struct. 98, 1–14.

Weaver, J.C., et al., 2007. Hierarchical assembly of the siliceous skeletal lattice of the hexactinellid sponge Euplectella aspergillum. J. Struct. Biol. 158 (1), 93–106.

Wei, K., et al., 2016. Design and analysis of integrated thermal protection system based on lightweight c/sic pyramidal lattice core sandwich panel. Mater. Des. 111, 435–444.

Wu, Q., et al., 2016. A novel strengthening method for carbon fiber composite lattice truss structures. Compos. Struct. 153, 585–592.

Xiong, J., et al., 2015. Advanced micro-lattice materials. Adv. Eng. Mater. 17 (9), 1253–1264.

Yang, W., Yue, Z., Xu, B., 2016. A hybrid elastomeric foam-core/solid-shell spherical structure for enhanced energy absorption performance. Int. J. Solids Struct. 92, 17–28.

Zhang, J., Qin, Q., Wang, T.J., 2013. Compressive strengths and dynamic response of corrugated metal sandwich plates with unfilled and foam-filled sinusoidal plate cores. Acta Mech 224 (4), 759.

Zhao, Z.L., et al., 2014. Mechanical properties of carbon nanotube ropes with hierarchical helical structures. J. Mech. Phys. Solids. 71, 64–83.

Zhao, L., et al., 2012. Hierarchical composite honeycombs. Mater. Des. 40, 124–129.

Zheng, X., et al., 2016. Multiscale metallic metamaterials. Nat. Mater. 15 (10), 1100–1106.

Zok, F.W., Latture, R.M., Begley, M.R., 2016. Periodic truss structures. J. Mech. Phys. Solids. 96, 184–203.